GENIORS

Research and Innovation Action (RIA)

This project has received funding from the European Union's Horizon 2020 research and innovation programme under grant agreement No 755171.

Start date : 2017-06-01 Duration : 48 Months
http://geniors.eu/

Molecular modeling of particular degradation mechanism of extracting and complexing agents

Authors : Pr. Jan JOHN (CTU), Ladislav Kalvoda (CTU), Lucie Celbová (CTU), Jaroslava Fojtíková (CTU), Tomá? Koubský (CTU), Jakub Lu?tinec (CTU), Bart Verlinden (SCK, CEN, KU Leuven, JARA), Piotr Kowalski (FZJ, JARA), Andreas Wilden (FZJ, JARA), Giuseppe Modolo (FZJ)

GENIORS - Contract Number: 755171

Project officer: Roger Garbil

Document title	Molecular modeling of particular degradation mechanism of extracting and complexing agents
Author(s)	Pr. Jan JOHN, Ladislav Kalvoda (CTU), Lucie Celbová (CTU), Jaroslava Fojtíková (CTU), Tomá? Koubský (CTU), Jakub Lu?tinec (CTU), Bart Verlinden (SCK, CEN, KU Leuven, JARA), Piotr Kowalski (FZJ, JARA), Andreas Wilden (FZJ, JARA), Giuseppe Modolo (FZJ)
Number of pages	44
Document type	Deliverable
Work Package	WP2
Document number	D2.5
Issued by	CTU
Date of completion	2020-06-09 15:38:53
Dissemination level	Public

Summary

The present Deliverable collects the theoretical studies carried out within GENIORS on the Molecular modelling of particular degradation mechanism of extracting and complexing agents. The results obtained are collected and divided according to the type of ligands used. The studies are focused on two types of extractants: i) CyMe4-BTBP and, in a larger extend, on hydrophilic DGA ligands (TMDGA, TEDGA, Me-TEDGA, Me2-TEDGA). Two approaches are applied: modelling of theoretical molecular stability indicators / descriptors and their juxtaposition to the known experimental data, and, based on the experimental findings, simulations of reaction pathways and analysis of their energetics. Both types of studies were mainly performed using ab-initio theoretical approaches either in ?gas phase?, i.e. on isolated molecule, or with inclusion of a contact with particular selected reactive species representing presence of acidic environment. In addition, classical molecular dynamics simulations were performed on thermodynamic ensembles representing tested solutions under realistic physical conditions and the produced trajectories analyzed. A large amount of simulated data has been collected and is discussed with aim to verify adequacy of the particular descriptor for the analyzed system (molecular model, reaction pathway) and through this comparison deepen the knowledge about the studied extraction systems and radiolytic processes and further improve the accuracy of applied modelling tools.

Approval

Date	By
2020-06-09 16:19:15	Dr. Hitos GALAN (CIEMAT)
2020-06-09 16:25:43	Mr. Andreas GEIST (KIT)
2020-06-12 18:05:36	Mr. Stéphane BOURG (CEA)

CONTENT

This project has received funding from the EURATOM research and training programme 2014-2018 under grant agreement No 755171. The content of this deliverable reflects only the author's view. The European Commission is not responsible for any use that may be made of the information it contains.

CONTRIBUTIONS

The report combines contributions of two project partners: Czech Technical University in Prague (CTU) and Forschungszentrum Jülich GmbH (FZJ). Results achieved by the CTU team compose the Sections 1.1 – 1.4, 2.1.1 – 2.1.6, 2.1.8 and 2.2.1. Sections 2.1.7 and 2.2.2 are then based on results of the FZJ group.

ABSTRACT

The present Deliverable collects the theoretical studies carried out within GENIORS on the Molecular modelling of particular degradation mechanism of extracting and complexing agents. The results obtained are collected and divided according to the type of ligands used. The studies are focused on two types of extractants: i) CyMe4-BTBP and, in a larger extend, on hydrophilic DGA ligands (TMDGA, TEDGA, Me-TEDGA, Me_2-TEDGA).

Two approaches are applied: modelling of theoretical molecular stability indicators / descriptors and their juxtaposition to the known experimental data, and, based on the experimental findings, simulations of reaction pathways and analysis of their energetics. Both types of studies were mainly performed using ab-initio theoretical approaches either in "gas phase", i.e. on isolated molecule, or with inclusion of a contact with particular selected reactive species representing presence of acidic environment. In addition, classical molecular dynamics simulations were performed on thermodynamic ensembles representing tested solutions under realistic physical conditions and the produced trajectories analyzed.

A large amount of simulated data has been collected and is discussed with aim to verify adequacy of the particular descriptor for the analyzed system (molecular model, reaction pathway) and through this comparison deepen the knowledge about the studied extraction systems and radiolytic processes and further improve the accuracy of applied modelling tools.

1 $CyMe_4$-BTBP

This Section provides theoretical analysis of radiolytic degradation of 6,6'-bis(5,5,8,8-tetramethyl-5,6,7,8-tetrahydro-1,2,4-benzotriazin-3-yl)-2,2'-bipyridine ($CyMe_4$-BTBP) dissolved in 1-octanol. The proposed reaction pathway is motivated by the experimentally observed radiolysis products.

1.1 CONFORMATIONS

The free BTBP-type ligands are expected to adopt the 'trans' conformation (the molecule is close to C2h symmetry; trans-$CyMe_4$-BTBP in Figure 1.1), where the central bond between two pyridine rings comprises the center of symmetry; the 'cis' conformation (C2v point group) is less energetically favored. The results calculated for $CyMe_4$-BTBP confirmed such expectation: the 'cis' conformation is 5.7 kcal/mol higher in energy than the 'trans' conformation possessing the activation energy of the rearrangement of 8.1 kcal/mol. Accordingly, we further assume that majority of $CyMe_4$-BTBP molecules in the solution adopt the 'trans' conformation. The further investigation shows that also the torsion angle of the triazine-pyridine bonds plays a role in the total energy of the molecule. Turning of such bond by 180 degrees with respect to the complexing conformation (bond L; trans-$CyMe_4$-BTBP-L in Figure 1.1) causes the drop in energy of about 0.3 kcal/mol. Changing the torsion angle of the other triazine-pyridine bond has the same effect (see Table 1.1).

This project has received funding from the EURATOM research and training programme 2014-2018 under grant agreement No 755171. The content of this deliverable reflects only the author's view. The European Commission is not responsible for any use that may be made of the information it contains.

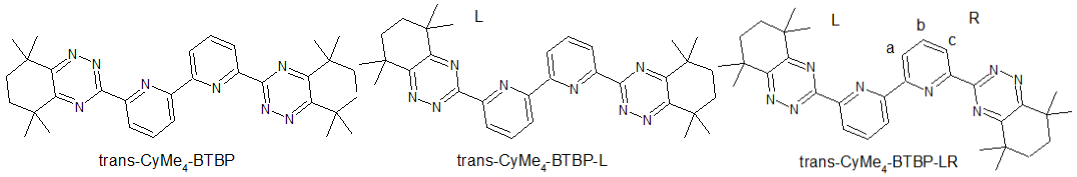

Figure 1.1 Chemical conformations of $CyMe_4$-BTBP. In the trans-$CyMe_4$-BTBP-LR structure, the probable position of the $C_8H_{17}O$ group are marked (a, b, and c)

Table 1.1 Energy of different $CyMe_4$-BTBP conformations

Molecular system	relative potential energy (kcal/mol)
trans-$CyMe_4$BTBP-LR	0.00
trans-$CyMe_4$BTBP-L	0.27
trans-$CyMe_4$BTBP	0.63
cis-$CyMe_4$BTBP	6.30

1.2 ADDUCTS

The HPLC-MS analysis of irradiated $CyMe_4$-BTBP solutions in 1-octanol showed that no degradation of the distribution ratios occurs and the resulting solution contains, in addition to the original $CyMe_4$-BTBP molecules, some adduct of 1-octanol to $CyMe_4$-BTBP [1].

It is thus plausible to expect that the core structure of adducts - involving the vicinity of the complexing nitrogen atoms - remains unchanged. Based on this assumption, we have selected three positions where the octanol can be attached to the $CyMe_4$-BTBP molecule (cf. trans-$CyMe_4$-BTBP-LR in Figure 1.1, positions ‘a’, ‘b’, ‘c’).

Before the geometrical optimization of the molecular structures, the pre-optimization by MD was performed. For each of the three products, six initial guess structures were made with different spatial orientations of the octanol carbon chains and the alcohol oxygen. For each of those initial guesses, six experimental cells were constructed reflecting the real experimental concentration conditions and equilibrated as canonical ensembles by MD.

After the MD simulations, the geometries of the tested molecules were optimized with low accuracy by DFT (BLYP / 6-31G(d,p)). Several energetically promising candidates were then optimized by the standard level of theory (B3LYP / 6-31G(d,p) / PCM, GD3BJ) with additional conformation investigations of the ring-ring torsion angles. By such procedure, the conformations with lowest possible energy (A, B, C) were found and geometrically optimized (Figure 1.2). The energy of formation was calculated and compared for all three structures. The obtained energetic difference between the structures A, B, C is small, possibly comparable to the energy of thermal vibrations (**Table** 1.2).

This project has received funding from the EURATOM research and training programme 2014-2018 under grant agreement No 755171. The content of this deliverable reflects only the author’s view. The European Commission is not responsible for any use that may be made of the information it contains.

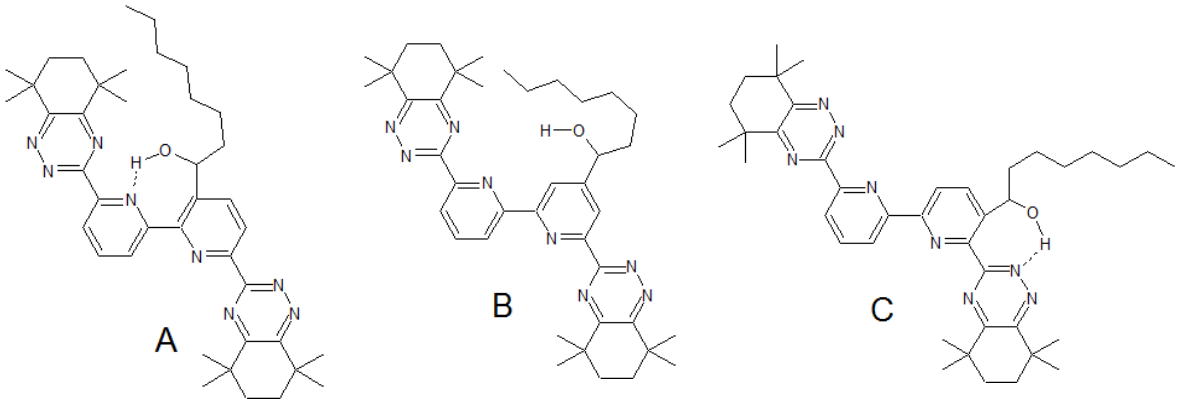

Figure 1.2 Chemical structures of the investigated adducts of $CyMe_4$-BTBP and 1-octanol

Table 1.2 Relative energy of formation calculated for optimized molecular structures

Molecular system	potential energy (kcal/mol)
product A	0.00
product B	3.25
product C	7.08

Surprisingly, the structure B (resulting from addition on the electron deficient carbon 'b') is not the one showing the lowest energy. In structures A and C, the possibility of an intramolecular H-bond creation between the alpha-hydroxyoctyl group and the neighboring triazine or pyridine group arises decreasing the energy of formation and working against the mesomeric effect mechanism. The calculated energy of mentioned intramolecular hydrogen bond in A and C amounts approximately 4.00 kcal/mol.

Thus, the structure A is found to be the most stable one and is therefore expected to the most frequently populated in solution. This result deserves a further analysis.

1.3 ORBITAL STRUCTURE

In the first place, the orbitals structure was analyzed. Assuming that the attachment of the alpha-hydroxyoctyl group runs through the nucleophilic substitution [2], we can make assumptions based on an analogical reaction of pure pyridine and a free radical. On pyridine, the nucleophilic substitution occurs predominantly at positions 2 (ortho) or 4 (para). Thanks to the inductive effect and mesomeric effect, carbon atoms at those positions have a deficiency of electron density, therefore they can more easily accommodate the partially occupied orbital of the attacking radical.

The electron deficiency can be seen from the orbital structure of pyridine (Figure 1.3). The preference of positions 'para' and 'ortho' can be expected from the increased concentration of the LUMO orbital in their vicinity.

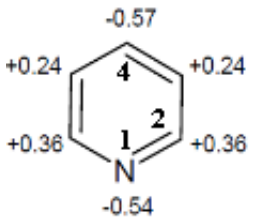

Figure 1.3. Concentration of LUMO orbital on pure pyridine (Gaussian, B3LYP, 6-31(d,p), PCM); atomic position numbers indicated

Transferred to the case of $CyMe_4$-BTBP and the alpha-hydroxyoctyl radical, the analogical position 'b' (Figure 1.4) would be more susceptible to the reaction than positions 'a' and 'c'. However, after calculation of the same properties for pure $CyMe_4$-BTBP, the circumstances are slightly different. At one pyridine ring, position 'b' contributes more to LUMO (ca. 4%) compared to 'a' and 'c', but at the other ring, position 'a' is the biggest

This project has received funding from the EURATOM research and training programme 2014-2018 under grant agreement No 755171. The content of this deliverable reflects only the author's view. The European Commission is not responsible for any use that may be made of the information it contains.

contributor by ca. 4%. Therefore, the possibility of higher concentration of LUMO at position 'a' can be one of the explanations why the consequent structure A is more stable, despite the expectations from pure pyridine.

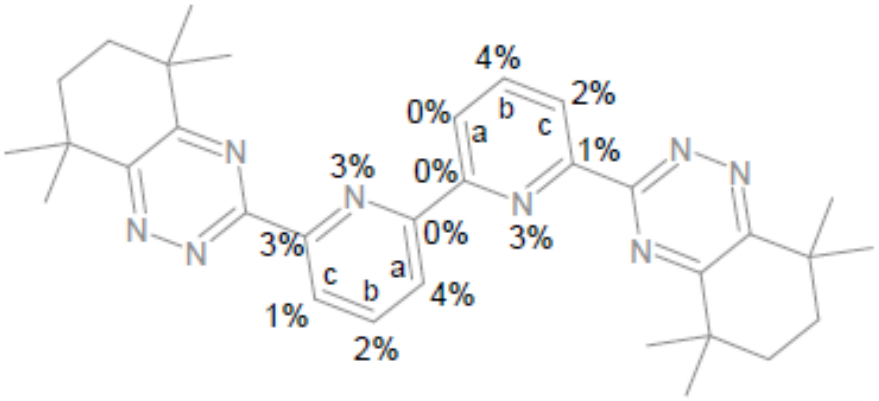

Figure 1.4. Contribution of selected atoms to LUMO of CyMe4-BTBP (Gaussian, B3LYP, 6-31(d,p), PCM)

Consequently, structures A and C can successfully compete with structure B. Besides that, the mentioned intramolecular H-bond probably already stabilizes the pre-reactive complex as well as the reaction intermediates.

1.4 REACTION MECHANISM

In the case of $CyMe_4$-BTBP we assume that the interaction of the solvent (1-octanol) with the ionizing radiation generates predominantly alpha-hydroxyoctyl radicals ($HOC•C_7H_{15}$). [3] The alpha-hydroxyoctyl radicals then react with the ligand molecules.

According to the mentioned assumptions, we suggested the full reaction mechanism of $CyMe_4$-BTBP and alpha-hydroxyoctyl radical in Figure 1.5. Our study is focused on the reaction steps Pre $\rightarrow$ 2 (Van der Waals pre-reactive complex of $CyMe_4$-BTBP and alpha-hydroxyoctyl radical $\rightarrow$ reaction intermediate of nucleophilic substitution) and 2 $\rightarrow$ 3 (hydrogen abstraction producing the final degradation product $CyMe_4$-BTBP-$CHOHC_7H_{15}$). The transition states related to these two reaction steps are optimized. Nevertheless, because these steps contain highly unstable radical species, their potential energy must lie very high compared to the full reaction chain occurring in the process. It is therefore necessary to analyze them in the context of the inevitable preceding and following reaction steps, such as generation of alpha-hydroxyoctyl radical (0 $\rightarrow$ 1), approaching of the alpha-hydroxyoctyl radical molecule to the $CyMe_4$-BTBP molecule, and the hypothetical final recombination of two hydrogen radicals. With steps 0 $\rightarrow$ 1, 1 $\rightarrow$ 2, and 3 $\rightarrow$ 4, the reaction path is bounded only by stable species and in its context, the examined reaction steps appear more meaningful.

The resulting reaction energy profile is presented in Figure 1.6. It can be clearly seen that energies of Pre (pre-reactive complex), TS1 (transition state), and 2 (reaction intermediate) determine the actual position where the octanol molecule attaches to the pyridine-ring of $CyMe_4$-BTBP.

As was already anticipated from the creation of intramolecular H-bonds and from the atomic contributions to LUMO orbital on $CyMe_4$-BTBP, the position 'b' (related to position ’para’ which is one of the preferred positions on pure pyridine) and product B is not the preferred one. Its pre-reactive complex (Pre) has ca. 29.98 $kJ·mol^{-1}$ higher formation energy than those of A and C, and the reaction intermediate (2) is even 10.98 $kJ·mol^{-1}$ higher. The activation energy of 29.10 $kJ·mol^{-1}$ related to the TS1 of B is also the highest, compared to A and C. Therefore we conclude that product B is not the prevailing one.

This project has received funding from the EURATOM research and training programme 2014-2018 under grant agreement No 755171. The content of this deliverable reflects only the author’s view. The European Commission is not responsible for any use that may be made of the information it contains.

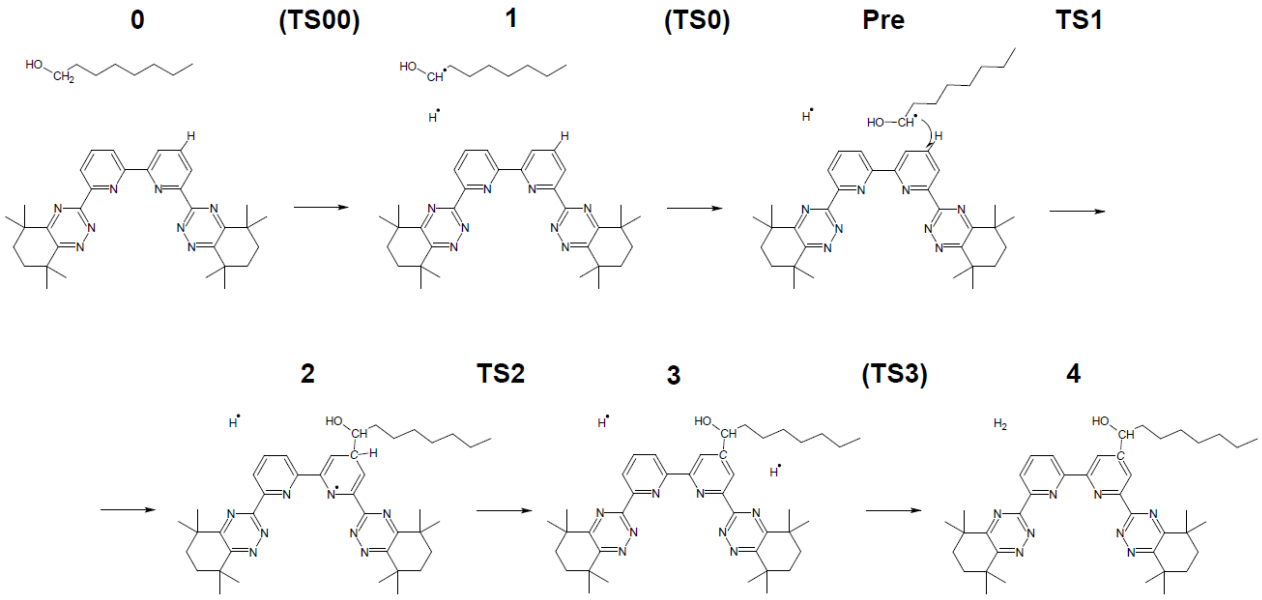

Figure1. 5. Full suggested reaction pathway of generation of the expected degradation product CyMe4-BTBP-CHOHC7H15; the transition states in brackets not optimized

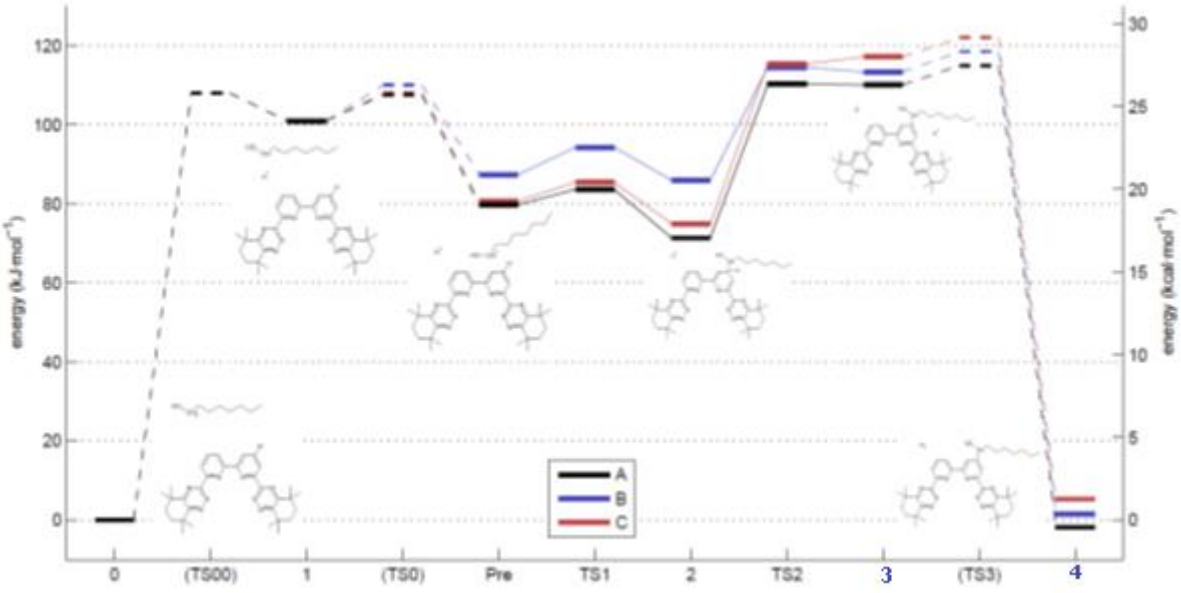

Figure 1.6. Energy profiles of the tested radical degradation reactions for CyMe4-BTBP with alpha-hydroxyoctyl radical at positions `a', `b', and `c' on pyridine ring, resulting in reaction products A, B, and C; calculated with Gaussian / B3LYP

Path A stands lowest in the total potential energy of TS2 compared to other reaction paths. Taking those facts into account, we keep the earlier mentioned preference for the reaction at position 'a' leading to product A.

The energies of reaction step 3 and transition state TS2 can seem to be surprisingly high. However, we must keep in mind that the step 2 → 3 produces a very reactive species, a hydrogen radical. The long-term existence of such species is very improbable and therefore, the extremely high resulting energies are understandable. In

This project has received funding from the EURATOM research and training programme 2014-2018 under grant agreement No 755171. The content of this deliverable reflects only the author's view. The European Commission is not responsible for any use that may be made of the information it contains.

reality, the reactive radicals react and decrease the energy of the system very quickly. This is also the reason why the whole picture of reaction steps 1 → 4 is important.

After analysis of the TS structures and energies, formation energies of the reaction intermediates, and formation energies of reaction products, we suggest that the degradation product A is the most preferred one. The conclusion is supported by the following findings:

- Formation energy of the product A is the lowest one (step 3 in the reaction path, cf. Table 1.2)
- Energy of its intermediate (2) is ca 63.64 kJ·mol^{-1} lower than that of B and C
- Activation energy of the position-determining step (TS1) amounting 16.54 kJ·mol^{-1} is the lowest on compared to products B and C.

The following reasons are then behind the site-preferences proposed above:

- Possibility of intramolecular H-bonds formation which is common for the products A and C and stabilizes the pre-reactive complex Pre
- The concentration of LUMO at position 'a' on CyMe$_4$-BTBP is higher compared to positions 'b' and 'c', in contrary to the standard situation of pure pyridine. This lowers the energy barrier of TS1 and stabilizes the corresponding intermediate 2.

2 DGA

A well-studied family of molecules for the separation of trivalent actinides and lanthanides from other fission products are diglycolamides (DGAs). The general molecular structure is shown in Figure 2.1.

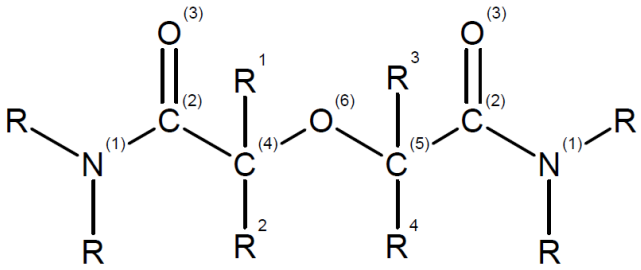

Figure 2.1: General structure of DGAs with the atom indices indicated

DGAs have been playing an important role in many partition processes for spent nuclear fuel.[4-5] In particular, the molecule with two linear octyl chains (marked as 'R' in Figure 2.1) on both nitrogen atoms, *N,N,N',N'*-tetraoctyl diglycolamide (TODGA), has been studied intensively for the purpose of solvent extraction [6]. Since then, it has been used in processes such as EURO-GANEX [7-9] and SANEX [10-13]. Later on, water soluble DGAs with shorter side R-chains have been prepared and tested, too (Table 2.1) [14].

Table 2.1: Studied DGA derivatives

Abbreviation	Chemical formula	Molecular weight (Da)	Name of the compound
TMDGA	$C_8H_{16}N_2O_3$	188.23	*N,N',N,N'*-tetramethyl-diglycolamide
TEDGA	$C_{12}H_{24}N_2O_3$	244.34	*N,N',N,N'*-tetraethyl-diglycolamide
Me-TEDGA	$C_{13}H_{26}N_2O_3$	258.36	2-(2-(diethylamino)-2-oxoethoxy) -*N,N'*-diethylpropanamide
Me$_2$-TEDGA	$C_{14}H_{28}N_2O_3$	272.39	2,2'-oxybis(*N,N'*-diethylpropanamide)
TODGA	$C_{36}H_{72}N_2O_3$	581.98	*N,N,N',N'*-tetraoctyl diglycolamide
mTDDGA	$C_{46}H_{92}N_2O_3$	721.25	*modified* tetradecyl diglycolamide

Usage of TEDGA involves processes such as EXAm (Extraction of Americium) [15] or ALSEP (Actinide Lanthanide Separation) [16]. The role of TEDGA in these processes is an aqueous stripping agent and a hold back agent, i.e.,

This project has received funding from the EURATOM research and training programme 2014-2018 under grant agreement No 755171. The content of this deliverable reflects only the author's view. The European Commission is not responsible for any use that may be made of the information it contains.

TEDGA makes more preferably complexes with Curium (Cm) or other lanthanide ions (Ln) than with Americium (Am). Subsequently, the selectivity ratios Am/Cm and Am/Ln of the other extractant used in the organic phase is higher. For example, in the EXAM process, DMDOHEMA molecule is used in place of extractant [17].

Considering the high radioactivity present in solutions containing spent nuclear fuel, the stability of organic components of a solvent extraction system is important for future applications in reprocessing. Therefore, it is required to obtain knowledge on this matter before upscaling newly developed processes. Concerning the DGAs, radiolysis experiments were at first conducted on lipophilic TODGA (18-20, 45] and its methylated derivatives [21-22]. Experimentally, solutions of DGAs in *n*-dodecane were irradiated with a gamma source and analyzed afterwards. Using techniques such as High Performance Liquid Chromatography coupled with Mass Spectrometry (HPLC-MS), the stability of extractant under ionizing irradiation can be determined on a quantitative level and degradation compounds can be identified. The identification of problematic radiolysis products is crucial to understand and ensure the long-term performance of a solvent in a solvent extraction process and its recycling. Therefore, the identified radiolysis products were synthesized and their extraction properties were studied individually [22, 45].

Multiple experimental works were also focused on investigating the radiolytic and hydrolytic stability of hydrophilic DGA-type ligands. This report largely relates to the studies by Wilden et al. [23] and Horne et al [24] dealing with the representatives of the DGA family listed in Table 2.1. Their hydrolysis and radiolysis were investigated separately, because the hydrolysis of TEDGA caused by nitric acid appears to occur by multiple mechanisms during the experiments. The rate of the hydrolysis was so remarkable that radiolysis needed to be at first investigated in pure water [23]. The DGA samples were irradiated to target the absorbed doses from 0 to 150 kGy at 23 $\pm$ 2 ^{o}C [23]. After the irradiation, the samples were analyzed by HPLC-MS. Kinetics measurements revealed fast rate constants for DGA reactions with the hydroxyl radical $^{\bullet}$OH, suggesting its importance in the mechanism of their radiolytic degradation in water. A decrease in dose constants with increasing molecular weight of DGAs indicated that the most important degradation mechanisms of the radical reaction are an electron transfer and a hydrogen abstraction. Wilden et al. concludes that the radiolytic stability increases for the studied molecules in the following order: TMDGA < TEDGA < Me-TEDGA $\leq$ Me_2-TEDGA [23].

The study of Horne et al. [24] were conducted on hydrophilic DGAs (Table 2.1) dissolved in concentrated aqueous nitrate solution with a neutral pH value. The experimental setup was similar to that one used by Wilden et al.[23]. Horne and coworkers demonstrated that (i) the studied hydrophilic DGAs undergo a first-order decay with an average dose constant of (-3.18 $\pm$ 0:23) x 10^{-6} Gy^{-1}; (ii) the observed degradation product distributions are similar to those found under pure water conditions, except for the appearance of NOx adducts; and (iii) the radiolysis process is likely driven by hydroxyl and nitrate radical oxidation chemistry moderated by secondary degradation products scavenging the reactions [24]. As a whole, similar to their lipophilic analogs, the radiolysis of hydrophilic DGAs in concentrated, aqueous nitrate solutions is significantly slower and less structurally sensitive than the same process under pure water conditions. Acid hydrolysis, not radiolysis, is thus expected to limit the useful lifetime of these extractants [24].

Since the complexity of processes related to the radiolysis of extraction ligands, application of theoretical modelling approaches focused on determination and evaluation of the theoretical stability descriptors relating to the tested ligands and the decay reaction kinetics of these is invaluable. For DGAs, such studies were performed by Koubský *et al.*[25-26]; studies dealing with different ligands have been recently published also by other groups (e.g. [27-28]). The calculated electronic structure parameters involved molecular orbitals, Fukui functions and Fukui charges, partial atomic charges, bond orders and electrostatic potential (ESP) distributions. Following these studies, Section 2.1 of this report starts with the theoretical stability descriptors calculated for the hydrophilic DGAs derivatives (Table 2.1) considered in four different model environments, one representing

This project has received funding from the EURATOM research and training programme 2014-2018 under grant agreement No 755171. The content of this deliverable reflects only the author's view. The European Commission is not responsible for any use that may be made of the information it contains.

a pure water, and the remaining three simulating the nitric acid influence by addition of one of the following groups to ligand structure: H^+, H_3O^+ and HNO_3. Due to the generally low concentrations of ligand in solvents, it is plausible to assume an indirect radiolysis mechanism: the degradation pathway starts with the radiolysis of solvent molecules, and products of these reactions interact then with ligand molecules causing their degradation. In the remaining text, we'll refer primarily to the following two possible decay mechanisms: a radical attack initiated by a hydrogen abstraction, and an electrophilic attack [23, 25-26].

Important information about a molecular electronic system provide the bond dissociation energy (BDE) values giving us the energy needed to be spent in order to homolytically cleave the intramolecular bonds. For different types of amide ligands, the method of BDE calculation was proposed and performed by Drader et al. [27]. In the next part of Section 2.1, the BDE values are first overviewed for TEDGA and its derivatives, and then influence of a side chain (R) length analyzed.

The last part of Section 2.1 provides the results obtained in testing application of conformation analysis to evaluation of molecular stability. The derived stability descriptors are obtained from statistical analysis of temporal trajectories produced by classic molecular dynamics simulations on canonic ensembles containing aqueous solutions of the studied ligands.

2.1 STABILITY DESCRIPTORS

2.1.1 MODELS OF LIGANDS WITH ACID

Initial geometries for all tested ligands were generated using the ground state geometry from [26] combined with the specific particle representing the nitric acid. For each acid model and each ligand, eight input geometries were created and optimized. Creation of hydrogen bonds was observed in the case of H^+ acid model for all ligands. For TMDGA, TEDGA and Me_2-TEDGA, the hydrogen bond is located between the H^+ cation (bonded to one of the carbonyl oxygen) and the ether oxygen (cf. Figure 2.2 (a)). For TEDGA, the length of this hydrogen bond is 1.899 Å. For Me-TEDGA, the H^+ cation is bonded to one of the amide nitrogen, consequently two hydrogen bonds are observed. The first one is between the H^+ and the ether oxygen (length 2.279 Å), and the second one between the H^+ and the carbonyl oxygen attached to the other amide group than the H^+ cation (length 1.589 Å; Figure 2.5 (b)).

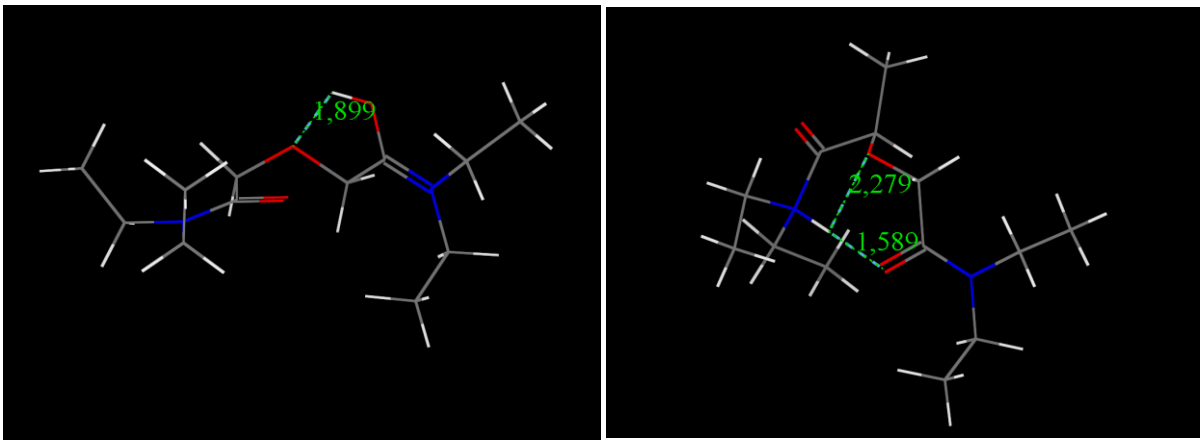

(a) (b)

Figure 2.2 TEDGA (a) and Me_2-TEDGA (b) structures of lowest energy showing presence of hydrogen bonds. H^+ acid model

This project has received funding from the EURATOM research and training programme 2014-2018 under grant agreement No 755171. The content of this deliverable reflects only the author's view. The European Commission is not responsible for any use that may be made of the information it contains.

The HNO_3 molecule is bonded to the carbonyl oxygen trough the hydrogen atom of the nitric acid molecule. No other binding locations of nitric acid molecule to the tested ligands are found (Figure 2.3).

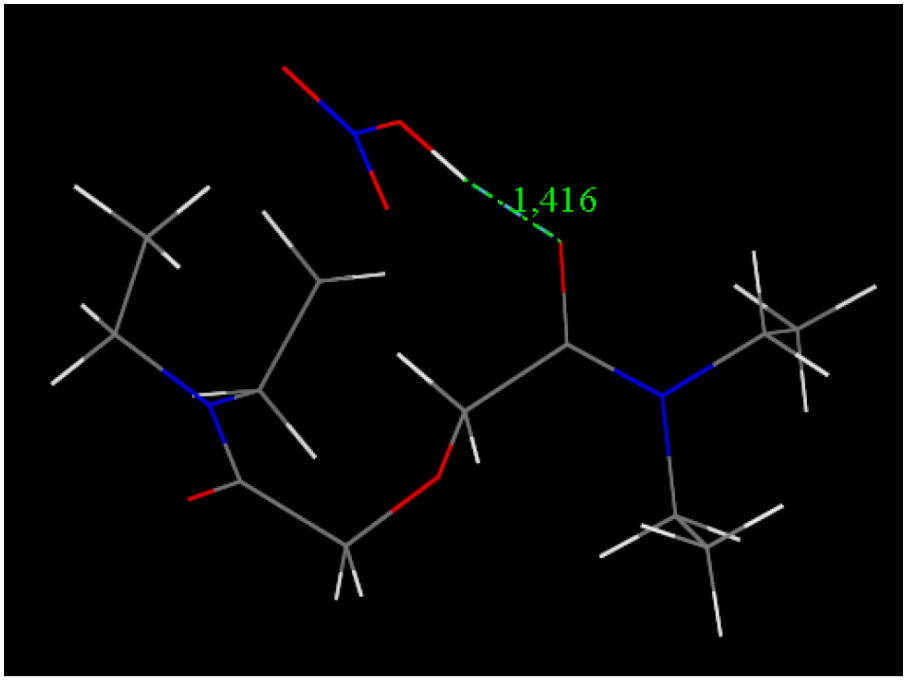

Figure 2.3 Hydrogen bridge between TEDGA and HNO_3; HNO_3 acid model; minimal total energy configuration

The obtained geometries of the studied ligands optimized within all applied acid models are then used in the subsequent calculations of electron density properties.

2.1.2 MOLECULAR ORBITALS

The HOMO-LUMO gap relates to chemical hardness and kinetic stability of a molecule. A hard molecule has a large gap and a soft one has a small gap. Generally, a lower HOMO-LUMO gap value implies a lower value of electronic excitation energy. Molecules with a small gap are more reactive than these with a larger gap [29-30]. HOMO-LUMO gap of TODGA and its methylated derivatives TWE-14 and TWE-21 was already analyzed in our previous study [25]. The resulting gap energies and trends were found to be remarkably sensitive to the level of theory applied.

Table 2.2 shows the calculated HOMO-LUMO gap energies obtained for the studied hydrophilic DGAs models. Table 2.3 shows then the values of gap between HOMO(DGA^-) and LUMO($^{\bullet}OH$) that relates to a degradation reaction initiated by hydroxyl radical and involving electron transfer.

Table 2.2 HOMO-LUMO gap energy (kJ/mol) calculated for the studied hydrophilic DGAs models (Gaussian, B3LYP, 6-31G(d,p), GD3BJ, NBO, PCM)

acid model	TMDGA	TEDGA	Me-TEDGA	Me_2-TEDGA
no acid	637	629	640	646
H^+	514	566	515	501
H_3O^+	680	672	670	670
HNO_3	483	483	481	420

This project has received funding from the EURATOM research and training programme 2014-2018 under grant agreement No 755171. The content of this deliverable reflects only the author's view. The European Commission is not responsible for any use that may be made of the information it contains.

Table 2.3 HOMO(DGA^-)-LUMO($^\bullet OH$) gap energy (kJ/mol) calculated for the studied hydrophilic DGAs models (Gaussian, B3LYP, 6-31G(d,p), GD3BJ, NBO, PCM)

acid model	TMDGA	TEDGA	Me-TEDGA	Me_2-TEDGA
no acid	227	226	225	218
H^+	250	264	293	248
H_3O^+	298	296	295	306
HNO_3	231	230	228	220

Apparently, the gap energies calculated for all considered models do not show any clear trend and cannot be easily correlated with the experimental data. This result confirms the previously observed insufficiency of the HOMO-LUMO gap energy in place of DGAs radiolytic stability indicator.

2.1.3 FUKUI FUNCTIONS AND FUKUI CHARGES

With regard to the considered decay mechanisms, two types of Fukui function (FF) are analyzed: radical FF and electrophilic FF. The radical FF is relevant for the degradation mechanism based on abstraction of the hydrogen atom on the ether group. The electrophilic FF is then instrumental for the degradation mechanisms beginning with the electron transfer from ligand molecule to the adjacent $^\bullet OH$ free radical. The calculated FF values are mapped on the 0.017 e/$Å^3$ iso-surface of molecule electron density. From the point of practical analysis and discussion of the results however, the volumetric FFs are difficult to treat due to their spatially delocalized nature. Introduction of atomically-condensed form of FFs called Fukui charges (FCs) removes this drawback. The FCs presented below are based on the Hirshfeld population analysis considered to be more relevant and less basis-set dependent than the alternative Mulliken population analysis.

RADICAL FUKUI FUNCTIONS

In the case of the lipophilic DGAs, the radical FF has proven to be a good descriptor for identifying the sites susceptible to a reaction with radicals [25]. For all the models of hydrophilic DGAs tested here, the main maximum of radical FF appears in vicinity of the hydrogen atoms bonded to the ether group. The trend observed for the tested ligands (Figure 2.4) is in concert with the experimental stability studies. For the acid models, the trend is preserved and the differences between individual derivatives are becoming even more resolved (remarkable especially for the H^+ and H_3O^+ models).

In all studied cases, the maxima of the radical FF close to the amide group are also evident suggesting susceptibility of the studied structures to radical attack at this locations (Figure 2.5 – 2.9). As demonstrated by Figure 2.5 and Figure 2.9, this basic character of radical FF for DGAs is insensitive to the particular length of the peripheral alkyl chain as well as to the applied level of theory.

This project has received funding from the EURATOM research and training programme 2014-2018 under grant agreement No 755171. The content of this deliverable reflects only the author's view. The European Commission is not responsible for any use that may be made of the information it contains.

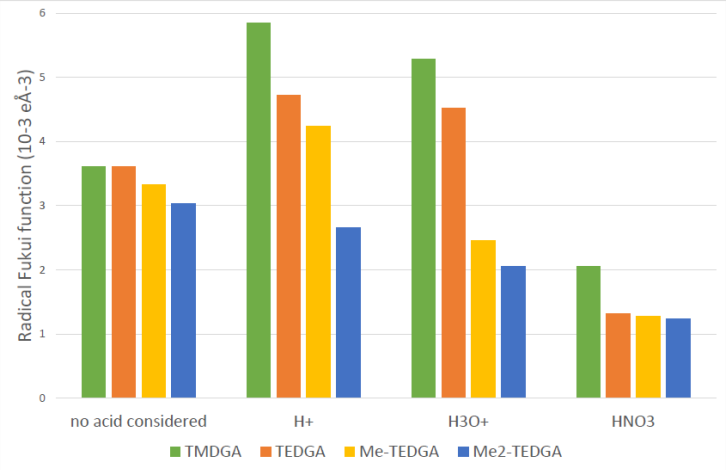

Figure 2.4 Maximum values of radical FF obtained for the studied hydrophilic DGA derivatives and acid models. The maximum located in vicinity of hydrogen atoms bonded to the ether group (red circle in Figure 2.5 a-d) (DMol^3, DNP, B3LYP, GD2, COSMO)

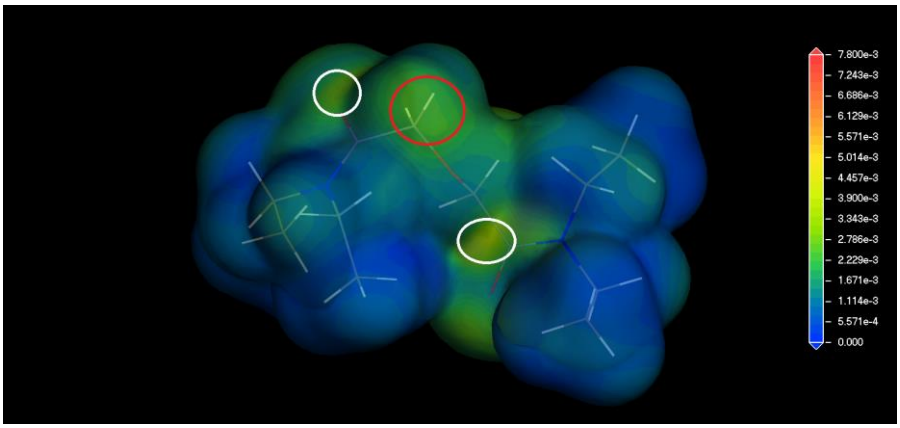

Figure 2.5 Radical FF calculated for TEDGA / no acid model; mapped on the 0.017 e/Å^3 iso-surface of electron density; red and white circles indicate maxima on the ether adjacent hydrogens and amide groups, respectively (DMol^3, DNP, B3LYP, GD2, COSMO)

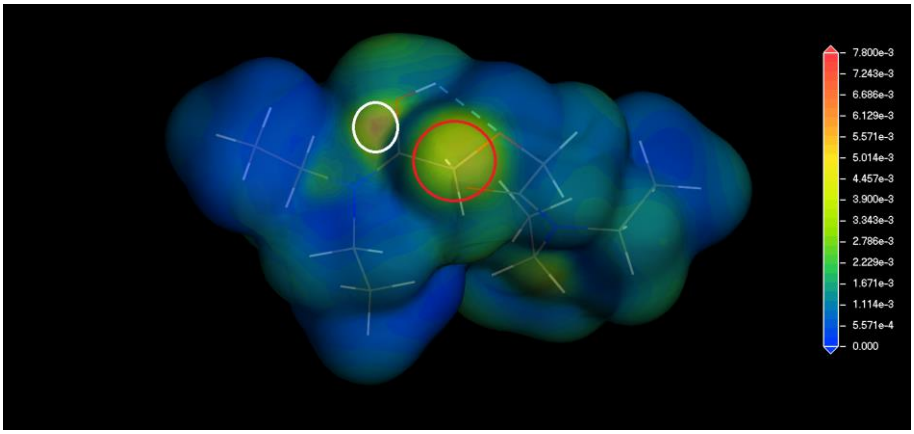

Figure 2.6 Radical FF calculated for TEDGA / H$^+$ acid model; mapped on the 0.017 e/Å^3 iso-surface of electron density; red and white circles indicate maxima on the ether adjacent hydrogens and amide groups, respectively (DMol^3, DNP, B3LYP, GD2, COSMO)

This project has received funding from the EURATOM research and training programme 2014-2018 under grant agreement No 755171. The content of this deliverable reflects only the author's view. The European Commission is not responsible for any use that may be made of the information it contains.

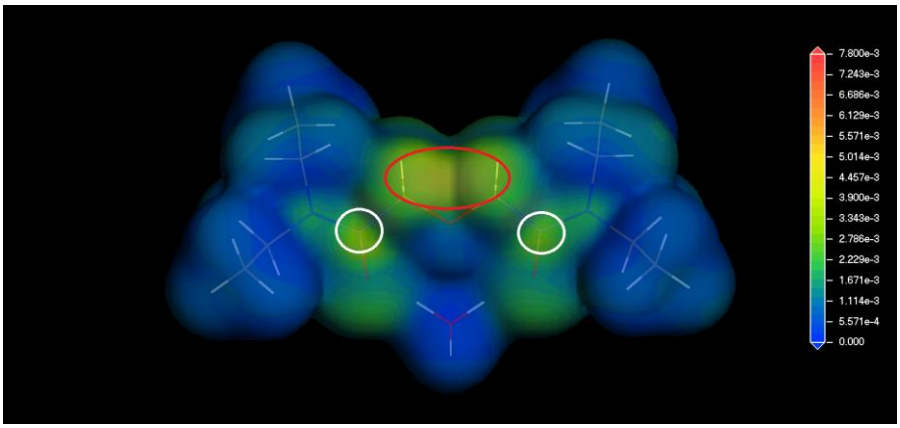

Figure 2.7 Radical FF calculated for TEDGA / H_3O^+ acid model; mapped on the 0.017 e/Å^3 iso-surface of electron density; red and white circles indicate maxima on the ether adjacent hydrogens and amide groups, respectively (DMol^3, DNP, B3LYP, GD2, COSMO)

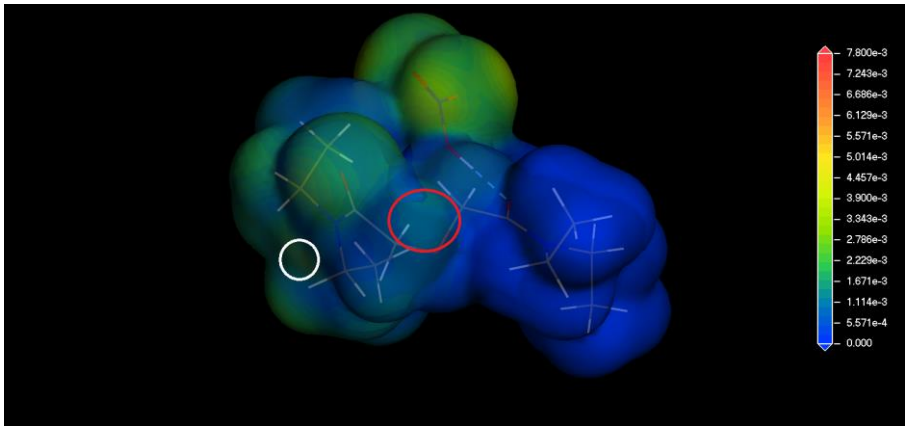

Figure 2.8 Radical FF calculated for TEDGA / HNO_3 acid model; mapped on the 0.017 e/Å^3 iso-surface of electron density; red and white circles indicate maxima on the ether adjacent hydrogens and amide groups, respectively (DMol^3, DNP, B3LYP, GD2, COSMO)

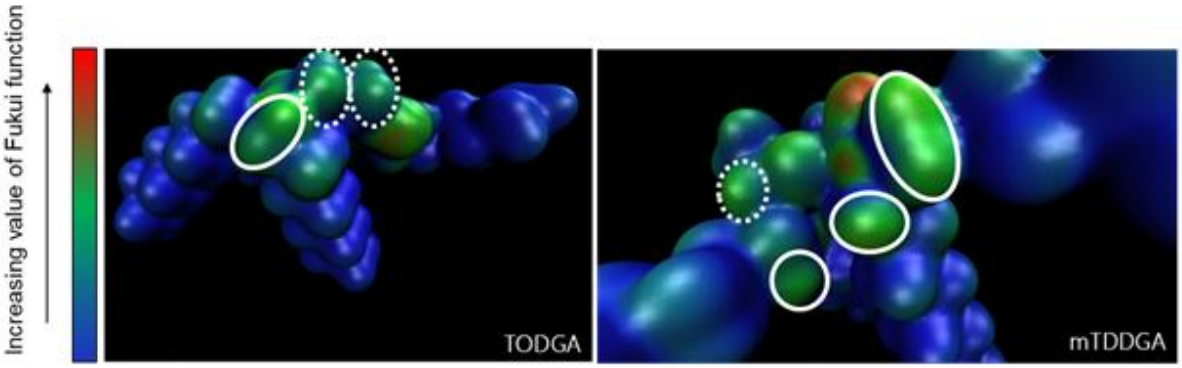

Figure 2.9 Radical FF calculated for TODGA and mTDDGA (dimethyl tetradodecyldiglycolamide); mapped on iso-surface of electron density; the dashed and full circles indicate maxima on the ether adjacent hydrogens and the hydrogen atoms on the alkyl chain, respectively (Quantum Espresso, DFT, PBE)

This project has received funding from the EURATOM research and training programme 2014-2018 under grant agreement No 755171. The content of this deliverable reflects only the author's view. The European Commission is not responsible for any use that may be made of the information it contains.

RADICAL FUKUI CHARGES

The radical FC calculated for the studied hydrophilic DGA derivatives and tested models are summarized in Tables 2.4 – 2.7. The values of FCs are averaged over the symmetry-related atoms. Labeling of the atoms introduced in Figure 2.1 is used.

Table 2.4 Radical FCs based on Hirshfeld population analysis / no acid model; atom labels after Figure 2.1 (DMol^3, DNP, B3LYP, GD2, COSMO)

atom	atom label	TMDGA	TEDGA	Me-TEDGA	Me_2-TEDGA
N	(1)	0.062	0.057	0.057	0.054
C	(2)	0.067	0.063	0.064	0.064
O	(3)	0.114	0.111	0.113	0.111
C	(4)	0.030	0.030	0.021	0.022
C	(5)	eq. (4)	eq. (4)	0.029	eq. (4)
O	(6)	0.037	0.033	0.033	0.036
H	R1	0.026	0.025	0.023	0.020
H	R2	eq. R1	eq. R1	-	-
H	R3	eq. R1	eq. R1	eq. R1	eq. R1
H	R4	eq. R1	eq. R1	eq. R1	-
H	avg. all Hs	0.021	0.014	0.013	0.012

Table 2.5 Radical FCs based on Hirshfeld population analysis / H^+ acid model; atom labels after Figure 2.1 (DMol^3, DNP, B3LYP, GD2, COSMO)

atom	atom label	TMDGA	TEDGA	Me-TEDGA	Me_2-TEDGA
N	(1)	0.096	0.072	0.049	0.070
C	(2)	0.071	0.068	0.076	0.065
O	(3)	0.097	0.074	0.108	0.088
C	(4)	0.020	0.019	0.013	0.009
C	(5)	eq. (4)	eq. (4)	0.018	eq. (4)
O	(6)	0.023	0.021	0.012	0.012
H	R1	0.025	0.024	0.022	0.014
H	R2	eq. R1	eq. R1	-	-
H	R3	eq. R1	eq. R1	eq. R1	eq. R1
H	R4	eq. R1	eq. R1	eq. R1	-
H	avg. all Hs	0.022	0.016	0.013	0.013

Table 2.6 Radical FCs based on Hirshfeld population analysis / H_3O^+ acid model; atom labels after Figure 2.1 (DMol^3, DNP, B3LYP, GD2, COSMO)

atom	atom label	TMDGA	TEDGA	Me-TEDGA	Me_2-TEDGA
N	(1)	0.065	0.061	0.062	0.060
C	(2)	0.072	0.070	0.068	0.064
O	(3)	0.079	0.078	0.078	0.083
C	(4)	0.025	0.025	0.018	0.015
C	(5)	eq. (4)	eq. (4)	0.020	eq. (4)
O	(6)	0.033	0.032	0.029	0.022
H	R1	0.031	0.029	0.019	0.015
H	R2	eq. R1	eq. R1	-	-
H	R3	eq. R1	eq. R1	eq. R1	eq. R1
H	R4	eq. R1	eq. R1	eq. R1	-
H	avg. all Hs	0.020	0.014	0.013	0.013

This project has received funding from the EURATOM research and training programme 2014-2018 under grant agreement No 755171. The content of this deliverable reflects only the author's view. The European Commission is not responsible for any use that may be made of the information it contains.

Table 2.7 Radical FCs based on Hirshfeld population analysis / HNO_3 acid model; atom labels after Figure 2.1 (DMol^3, DNP, B3LYP, GD2, COSMO)

atom	atom label	TMDGA	TEDGA	Me-TEDGA	Me_2-TEDGA
N	(1)	0.038	0.045	0.044	0.065
C	(2)	0.019	0.018	0.016	0.018
O	(3)	0.067	0.058	0.058	0.058
C	(4)	0.009	0.006	0.002	0.007
C	(5)	eq. (4)	eq. (4)	0.006	eq. (4)
O	(6)	0.022	0.007	0.004	0.007
H	R1	0.011	0.008	0.006	0.011
H	R2	eq. R1	eq. R1	-	-
H	R3	eq. R1	eq. R1	eq. R1	eq. R1
H	R4	eq. R1	eq. R1	eq. R1	-
H	avg. all Hs	0.012	0.009	0.008	0.008

High values of the radical FCs on N(1), C(2) and O(3) atoms correspond to the extremes of the volumetric radical FF on the amide group. Values of these FCs are not significantly changed in H^+ and H_3O^+ acid representations, but drop remarkable for the HNO_3 acid model. The possible reaction mechanism initiated in this area is unknown.

The most important area in the study of DGA radiolysis is the ether group. The radical FCs on the oxygen O(6) do not indicate any systematic trend with no acid present. However, under influence of acid, the value of FC for O(6) is decreasing with the molecular weight of ligand increasing for all three tested acid representations. Finally, with no acid present, the radical FCs values on C(4) and C(5) carbons indicate a descending tendency with the ligand molecular weight rising up. This phenomenon remains unchanged for all three acid representations.

The radical FCs on hydrogen atoms at positions R1 - R4 adjacent to C(4) and C(5) carbons are averaged (when there is a methyl group present at the given position, the FC value is not indicated). Since the ether group is the most likely site where the reaction with radical is initiated, these hydrogens are those that are likely to be abstracted by the incoming radical. Indeed, the calculated FCs values display in this case a falling trend conformal with the experimentally determined decay rate TMDGA > TEDGA > Me-TEDGA $\geq$ Me_2-TEDGA .

Considering the abstraction of the hydrogen adjacent to the ether group as the initiation of the degradation reaction, it must not be forgotten that in the case of methylated ligands the number of possible reaction centers (a hydrogen adjacent to the ether group at positions R1 -R4) is reduced up to one half, lowering thus correspondingly the probability of hydrogen abstraction for the methylated ligands, in accordance with the experimentally observed trend of the stability.

For TMDGA (as an exception among the studied ligands), products that correspond to the rupture of the C-O ether bond were not observed during the experiment [23]. The authors suggested that the abstraction of the hydrogen atom does not occur at the positions R1 - R4, but at the R chain. In order to verify this possibility, we've determined an average value of the radical FCs over all hydrogens in molecule and compare it with the radical FCs on hydrogens R1 - R4. In case of TMDGA / no acid model (Table 2.4), the average value (0.021) is relatively close to the radical FCs on R1 - R4 (0.026). Thus, indeed, the probability of hydrogen abstraction from the ether group is comparable to the abstraction from any of the CH_3 groups. For the rest of tested DGAs and no acid model, the values of radical FCs at positions R1 - R4 (e.g. 0.025 for TEDGA) exceed the average value over all hydrogens significantly (0.014 is obtained for TEDGA). This findings suggests that for TEDGA and its

This project has received funding from the EURATOM research and training programme 2014-2018 under grant agreement No 755171. The content of this deliverable reflects only the author's view. The European Commission is not responsible for any use that may be made of the information it contains.

methylated derivatives, in contrary to TMDGA, the probability of the hydrogen abstraction from the ether group dominates over the abstraction from the side alkyl chains.

For the H^+ acid model, the radical FCs at positions R1 – R4 calculated for TMDGA (0.025) are even closer to the corresponding average value (0.022). For Me_2-TEDGA, the two values are low and nearly identical (0.014 vs. 0.013), suggesting likely an overall increase in the resistance against hydrogen abstraction mechanism. For the remaining two ligands, the difference persists (Table 2.5).

For the H_3O^+ acid representation, the small difference between the average value for all hydrogens and the value for hydrogens at positions R1 - R4 is not present for TMDGA, but it remains similar to H^+ acid model for Me_2-TEDGA (table 2.6). Finally, in frame of the HNO_3 acid model, the average values of radical FCs for all hydrogens are almost the same as the radical FCs for hydrogens at positions R1 - R4 for all the tested ligands (Table 2.7).

In general, the inclusion of the acid influence leads to reduction of the radical FCs mainly on the ether group, and does not significantly change the basic stability trends observed with no acid present; in case of the H^+ acid model, the differences among the ligands are even deepened.

ELECTROPHILIC FUKUI FUNCTION - ELECTRON TRANSFER

The second considered reaction mechanism – electrophilic attack - consists in removal of electron from the ligand under influence of an electrophile, such as oxidizing radical $^{\bullet}OH$, occurring presumably in vicinity of one of the amide groups [23]. Such assumption is supported by the calculated electrophilic FCs (Table 2.8).

Table 2.8 Electrophilic FCs based on Hirshfeld population analysis / no acid model; atom labels after Figure 2.1 (DMol^3, DNP, B3LYP, GD2, COSMO)

atom	atom label	TMDGA	TEDGA	Me_TEDGA	Me_2_TEDGA
N	(1)	0.062	0.079	0.075	0.069
C	(2)	0.067	0.035	0.035	0.033
O	(3)	0.114	0.121	0.122	0.119
C	(4)	0.030	0.014	0.012	0.014
C	(5)	eq. (4)	eq. (4)	0.011	eq. (4)
O	(6)	0.037	0.025	0.025	0.044
H	R1	0.026	0.017	0.016	0.017
H	R2	eq. R1	eq. R1	_	_
H	R3	eq. R1	eq. R1	eq. R1	eq. R1
H	R4	eq. R1	eq. R1	eq. R1	_
H	avg. all Hs	0.022	0.015	0.014	0.013

Electrophilic FCs at the N (1), C (2) and O (3) amide atoms are notably greater than these found for all other atoms and all tested DGAs. The tendency of electrophilic FCs on C(2) is conformal with the expected stability trend, in contrast to the values found at N(1) and O(3) showing a slight increase when going from TMDGA towards Me-TEDGA and then a modest drop for Me_2-TEDGA. These results seem to suggest a key role of the amide carbon C(2) in possible stabilization of the TEDGA and its derivatives against electrophilic attack on the amide group. For the ether group (C(4), C(5), O(6)), the electrophilic FCs values for TMDGA are higher than for the TEDGA and its derivatives. For the latter, FCs do not significantly differ (with the exception of isolated increase at O(6) for Me_2-TEDGA), what could again (together with the trend on C(2)) be likely correlated to the different behavior of TMDGA during the experiment reported by Wilden at al. [23].

This project has received funding from the EURATOM research and training programme 2014-2018 under grant agreement No 755171. The content of this deliverable reflects only the author's view. The European Commission is not responsible for any use that may be made of the information it contains.

The electrophilic FCs calculated with inclusion of the acid models show considerable changes at positions of the amide group atoms (Table 2.9 – 2.11).

Table 2.9 Electrophilic FCs based on Hirshfeld population analysis / H^+ acid model; atom labels after Figure 2.1 (DMol^3, DNP, B3LYP, GD2, COSMO)

atom	atom label	TMDGA	TEDGA	Me-TEDGA	Me_2-TEDGA
N	(1)	0.086	0.089	0.085	0.086
C	(2)	0.041	0.031	0.035	0.031
O	(3)	0.117	0.090	0.087	0.111
C	(4)	0.016	0.012	0.002	0.004
C	(5)	eq.(4)	eq. (4)	0.017	eq. (4)
O	(6)	0.033	0.023	0.012	0.007
H	R1	0.018	0.015	0.016	0.009
H	R2	eq. R1	eq. R1	-	-
H	R3	eq. R1	eq. R1	eq. R1	eq. R1
H	R4	eq. R1	eq. R1	eq. R1	-
H	avg. all Hs	0.020	0.015	0.015	0.013

Table 2.10 Electrophilic FCs based on Hirshfeld population analysis / H_3O^+ acid model; atom labels after Figure 2.1 (DMol^3, DNP, B3LYP, GD2, COSMO)

atom	atom label	TMDGA	TEDGA	Me-TEDGA	Me_2-TEDGA
N	(1)	0.082	0.078	0.079	0.074
C	(2)	0.030	0.032	0.034	0.025
O	(3)	0.073	0.079	0.081	0.062
C	(4)	0.017	0.019	0.008	0.009
C	(5)	eq. (4)	eq. (4)	0.019	eq. (4)
O	(6)	0.065	0.052	0.033	0.026
H	R1	0.023	0.024	0.018	0.015
H	R2	eq. R1	eq. R1	-	-
H	R3	eq. R1	eq. R1	eq. R1	eq. R1
H	R4	eq. R1	eq. R1	eq. R1	-
H	avg. all Hs	0.021	0.015	0.013	0.014

Table 2.11 Electrophilic FCs based on Hirshfeld population analysis / HNO_3 acid model; atom labels after Figure 2.1 (DMol^3, DNP, B3LYP, GD2, COSMO)

atom	atom label	TMDGA	TEDGA	Me-TEDGA	Me_2-TEDGA
N	(1)	0.067	0.087	0.086	0.082
C	(2)	0.035	0.035	0.031	0.029
O	(3)	0.127	0.111	0.112	0.108
C	(4)	0.017	0.010	0.010	0.006
C	(5)	eq. (4)	eq. (4)	0.002	eq. (4)
O	(6)	0.044	0.013	0.006	0.021
H	R1	0.020	0.013	0.010	0.015
H	R2	eq. R1	eq. R1	-	-
H	R3	eq. R1	eq. R1	eq. R1	eq. R1
H	R4	eq. R1	eq. R1	eq. R1	-
H	avg. all Hs	0.020	0.015	0.014	0.013

This project has received funding from the EURATOM research and training programme 2014-2018 under grant agreement No 755171. The content of this deliverable reflects only the author's view. The European Commission is not responsible for any use that may be made of the information it contains.

Difference of electrophilic FCs at the N(1) atom between TMDGA and remaining DGAs is diminished for H^+ and H_3O^+ acid models, but remain unchanged for the HNO_3 model. The higher values of electrophilic FSc at the carbon C(2) for TMDGA compared to remaining DGAs diminish or vanish with including the acid influence.

The most remarkable influence of the acid models is seen on the electrophilic FCs of the ether group atoms. While no significant difference is observed with no acid included (Table 2.8), a noticeable decrease occurs of the FCs values at the C(4), C(5), O(6) atoms and all H positions R1 – R4 for all acid models. Few exceptions are present, for example the O(6) oxygen within the H_3O^+ acid model. The observed decreasing trends are in agreement with the experimentally observed trend of the stability for all acid models.

Similarly to the situation without acid, the electrophilic FCs averaged over all hydrogen atoms are very close to the values at R1 - R4 positions for all acid representations, too. Thus, a similar electrophilic reactivity of all the tested DGAs molecules at these sites can be expected.

2.1.4 PARTIAL CHARGES

The partial charges were calculated for all considered models using the Natural population analysis method (Table 2.12 – 2.15). In general, the observed changes in atomic charges can be attributed to the choice of the acid model, depending in particular on the site of contact between the molecule and the particle representing the acid in the particular model as well as on the total charge of the model system. Let's recall that the total charge is zero for the HNO_3 acid model and +1e for the H^+ and H_3O^+ models.

The effect is here demonstrated for the H^+ acid model (Table 2.13) on the charges calculated for the N(1) or C(2) atoms. For Me-TEDGA, where the H^+ cation is bonded to a different location of the ligand than in the case of the remaining ligands, the partial charge on the N(1) atom is -0.495 for Me-TEDGA, but it is -0.415 e for TEDGA or -0.410 e for Me_2-TEDGA. Thus, in contrast to other two acid models, the H^+ model shows a remarkable difference from the acid-free situation.

Table 2.12 Partial charges based on the Natural population analysis / no acid model; atom labels after Figure 2.1 (Gaussian, B3LYP, GD3BJ, 6-31G(d,p), NBO, PCM)

atom	atom label	TMDGA	TEDGA	Me-TEDGA	Me_2-TEDGA
N	(1)	-0.455	-0.465	-0.465	-0.464
C	(2)	0.666	0.668	0.672	0.681
O	(3)	-0.673	-0.676	-0.679	-0.682
C	(4)	-0.195	-0.192	0.011	0.016
C	(5)	eq. (4)	eq. (4)	-0.188	eq. (4)
O	(6)	-0.589	-0.588	-0.596	-0.607

Table 2.13 Partial charges based on the Natural population analysis / H^+ acid model; atom labels after Figure 2.1 (Gaussian, B3LYP, GD3BJ, 6-31G(d,p), NBO, PCM)

atom	atom label	TMDGA	TEDGA	Me-TEDGA	Me_2-TEDGA
N	(1)	-0.457	-0.415	-0.495	-0.410
C	(2)	0.687	0.698	0.722	0.683
O	(3)	-0.654	-0.670	-0.601	-0.659
C	(4)	-0.194	-0.190	0.011	0.009
C	(5)	eq. (4)	eq. (4)	-0.193	eq. (4)
O	(6)	-0.601	-0.583	-0.588	-0.599

This project has received funding from the EURATOM research and training programme 2014-2018 under grant agreement No 755171. The content of this deliverable reflects only the author's view. The European Commission is not responsible for any use that may be made of the information it contains.

Table 2.14 Partial charges based on the Natural population analysis / H_3O^+ acid model; atom labels after Figure 2.1 (Gaussian, B3LYP, GD3BJ, 6-31G(d,p), NBO, PCM)

atom	atom label	TMDGA	TEDGA	Me-TEDGA	Me_2-TEDGA
N	(1)	-0.419	-0.429	-0.428	-0.423
C	(2)	0.711	0.712	0.716	0.707
O	(3)	-0.693	-0.693	-0.695	-0.698
C	(4)	-0.192	-0.188	0.022	0.020
C	(5)	eq. (4)	eq. (4)	-0.187	eq. (4)
O	(6)	-0.578	-0.577	-0.589	-0.593

Table 2.15 Partial charges based on the Natural population analysis / HNO_3 acid model; atom labels after Figure 2.1 (Gaussian, B3LYP, GD3BJ, 6-31G(d,p), NBO, PCM)

atom	Atom label	TMDGA	TEDGA	Me-TEDGA	Me_2-TEDGA
N	(1)	-0.435	-0.444	-0.444	-0.465
C	(2)	0.681	0.682	0.687	0.681
O	(3)	-0.683	-0.687	-0.690	-0.678
C	(4)	-0.194	-0.192	0.011	0.013
C	(5)	eq. (4)	eq. (4)	-0.188	eq. (4)
O	(6)	-0.587	-0.586	-0.595	-0.609

Increase of the charge on the ether O(6) oxygen accompanying introduction of methyl groups on the C(4) and C(5) atoms is observed with no acid present. The methyl group provides electron density to the surrounding atoms. Therefore, bonding of the methyl group on C(4) and C(5) atoms (synthesis of Me-TEDGA and Me_2-TEDGA) should protect the ether O(6)-C(4) and O(6)-C(5) bonds, i.e., these bonds are expected to have higher bond order than in the case with no methyl group attached. Surprisingly, this does not occur for the studied molecules (cf. Section 2.1.5 below). The partial charge on the ether oxygen O(6) increases as a result of methylation and remains nearly identical for TMDGA and TEDGA. The same situation was already observed in the case of TODGA and its derivatives [25]. The described phenomenon is not altered by introduction of the acid models, with exception of a small deviation occurring for H^+ acid model, where the charge at the oxygen O(6) is respectively -0.601 e and -0.583 e for TMDGA and TEDGA; the trend for TEDGA and its methylated derivatives remains unchanged.

In the acid-free model, the methylation results in a positive shift of the partial charges at C(4) and C(5) atoms. The same effect also happens for all considered acid models (cf. Table 2.13 – 2.15). Since chemical nature of these carbon atoms have been changed by introduction of the methyl group(s), it is not possible to regard these charge differences as indicative for any change in reactivity or other chemical property of the atoms.

2.1.5 BOND ORDERS

Bond orders provide a useful tool for investigating molecular stability. The Wiberg bond indices based on the natural bond orbital (NBO) theory are calculated for the acid-free situation and the tested acid models (Table 2.16 – 2.19).

This project has received funding from the EURATOM research and training programme 2014-2018 under grant agreement No 755171. The content of this deliverable reflects only the author's view. The European Commission is not responsible for any use that may be made of the information it contains.

Table 2.16 Wiberg bond indices / no acid model; atom labels after Figure 2.1 (Gaussian, B3LYP, GD3BJ, 6-31G(d,p), NBO, PCM)

bond	TMDGA	TEDGA	Me-TEDGA	Me_2-TEDGA
N(1)-C(2)	1.225	1.233	1.235	1.235
C(2)-O(3)	1.604	1.597	1.593	1.593
C(2)-C(4)	0.965	0.964	0.954	0.945
C(4)-O(6)	0.904	0.904	0.889	0.884
C(5)-O(6)	eq. C(4)-O(6)	eq. C(4)-O(6)	0.900	eq. C(4)-O(6)

Table 2.17 Wiberg bond indices / H^+ acid model; atom labels after Figure 2.1 (Gaussian, B3LYP, GD3BJ, 6-31G(d,p), NBO, PCM)

bond	TMDGA	TEDGA	Me-TEDGA	Me_2-TEDGA
N(1)-C(2)	1.355	1.368	1.076	1.371
C(2)-O(3)	1.408	1.372	1.688	1.393
C(2)-C(4)	0.986	0.982	0.972	0.961
C(4)-O(6)	0.895	0.908	0.895	0.880
C(5)-O(6)	eq. C(4)-O(6)	eq. C(4)-O(6)	0.913	eq. C(4)-O(6)

Table 2.18 Wiberg bond indices / H_3O^+ acid model; atom labels after Figure 2.1 (Gaussian, B3LYP, GD3BJ, 6-31G(d,p), NBO, PCM)

bond	TMDGA	TEDGA	Me-TEDGA	Me_2-TEDGA
N(1)-C(2)	1.322	1.328	1.332	1.339
C(2)-O(3)	1.446	1.442	1.439	1.427
C(2)-C(4)	0.982	0.982	0.971	0.958
C(4)-O(6)	0.913	0.914	0.892	0.895
C(5)-O(6)	eq. C(4)-O(6)	eq. C(4)-O(6)	0.914	eq. C(4)-O(6)

Table 2.19 Wiberg bond indices / HNO_3 acid model; atom labels after Figure 2.1 (Gaussian, B3LYP, GD3BJ, 6-31G(d,p), NBO, PCM)

bond	TMDGA	TEDGA	Me-TEDGA	Me_2-TEDGA
N(1)-C(2)	1.276	1.282	1.285	1.228
C(2)-O(3)	1.524	1.519	1.515	1.597
C(2)-C(4)	0.971	0.970	0.964	0.946
C(4)-O(6)	0.904	0.903	0.880	0.882
C(5)-O(6)	eq. C(4)-O(6)	eq. C(4)-O(6)	0.904	eq. C(4)-O(6)

Order of bonds within the ether group (C(4)-O(6) and C(5)-O(6)) is found to be the lowest one for all tested models and molecular systems, suggesting the ether bond to be the weakest one and to be the location, where the degradation mechanism is initiated. Decrease of the bonds indices with the increasing molecular weight of ligand is predicted, in disagreement with the experimentally observed trend of the stability. Although the additional electron density provided by methylation is located on the ether carbon C(4) and / or C(5) (cf. Section 2.1.4) the bond order C(4)-O(6) and / or C(5)-O(6) (based on the orbital overlap) does not increase. Similar findings was already reported for TODGA and its methylated derivatives [25]. As shown in [25], the bond orders alone cannot be used as decisive stability indicators. Only a complete analysis of all computed electronic properties and their collective understanding can be used for their reliable interpretation.

This project has received funding from the EURATOM research and training programme 2014-2018 under grant agreement No 755171. The content of this deliverable reflects only the author's view. The European Commission is not responsible for any use that may be made of the information it contains.

The prevailing trend of increasing bond order with the growing molecular weight of ligand is observed for the N(1)-C(2) bond for all tested models, with two exceptions in case of Me-TEDGA / H^+ and Me_2-TEDGA / HNO_3 acid models. In the first case, the reason is likely in difference in mutual position of TEDGA-Me and H^+ ion compared to other tested derivatives (cf. Section 2.1.4). The reason for the second deviation remains unknown. The N(1)-C(2) bond is supposed to play important role in the degradation mechanism based on the electron transfer initiation (electrophilic attack). The observed trend is conformal with the experimentally determined stability evolution.

2.1.6 ELECTROSTATIC POTENTIAL

The ESP is usually used to investigate intermolecular interactions and also to understand the interactions with electrophilic species. Negative local value of ESP implies that the corresponding location is more susceptible to a reaction with an electrophilic particle. The calculated ESP is mapped on the 0.017 e/Å^3 iso-surface of molecular electron density.

Results of the ESP calculations for acid-free state have been used as initial information while creating the systems with different acid representations. Since the particles representing the acid usually have a positive charge, places of negative ESP extremes are selected as the prospective starting positions.

Within each of the tested acid models, a similar ESP distribution is obtained irrespective the particular DGA derivative, as demonstrated in Figure 2.10 for the case of H^+ acid model. Some variations of the ESP distribution are observed when changing between different acid models; however, in all cases, two main locations of ESP extremes can be identified: the first one located at the carbonyl oxygens and the second one at the ether oxygen atom, as illustrated for TEDGA / H_3O^+ acid model in Figure 2.11. Location of these extremes agrees well with the values of partial charges calculated for these oxygen atoms (cf. Section 2.1.4).

In all acid models, other additional ESP extremes appeared, too. The most significant is found at the nitric acid molecule in case of the HNO_3 acid model. However, since these maxima usually appear on the acid-representing particle, outside of the ligand itself, we do not interpret them as an indicator related to stability of the ligand.

In sense of the experimentally determined mutual stability trend of the ligands, the analysis of ESP does not provide any simple guidance.

This project has received funding from the EURATOM research and training programme 2014-2018 under grant agreement No 755171. The content of this deliverable reflects only the author's view. The European Commission is not responsible for any use that may be made of the information it contains.

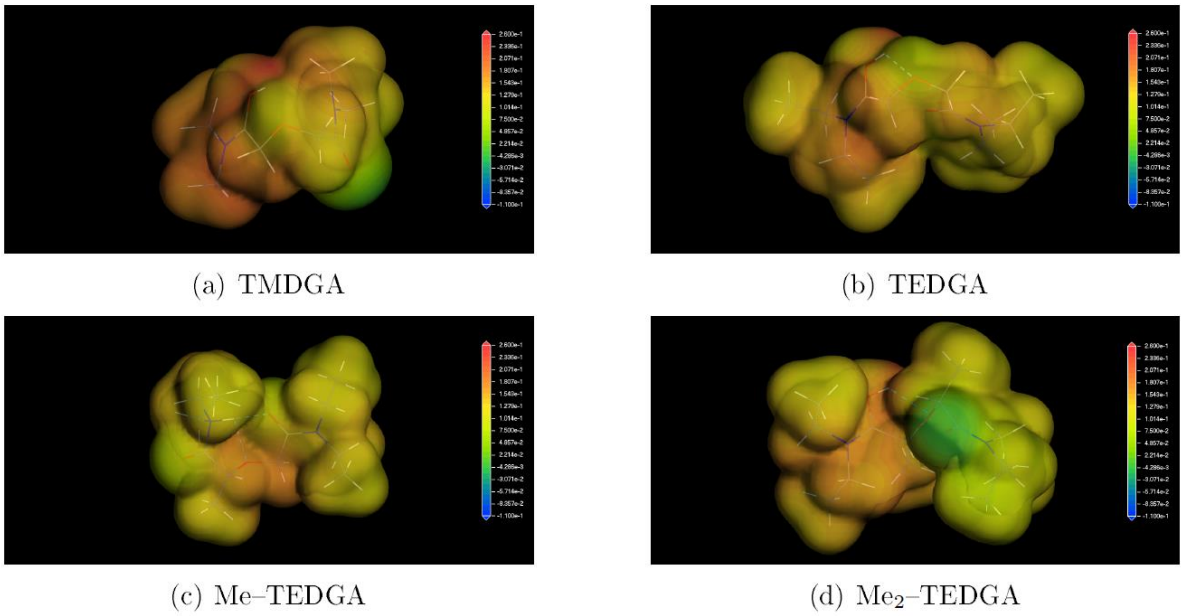

Figure 2.10 Electrostatic potential / H^+ acid model calculated for indicated DGA derivatives; ESP distribution mapped on 0.017 e/Å3 iso-surface of molecular electron density (DMol^3, DNP, B3LYP, GD2, COSMO)

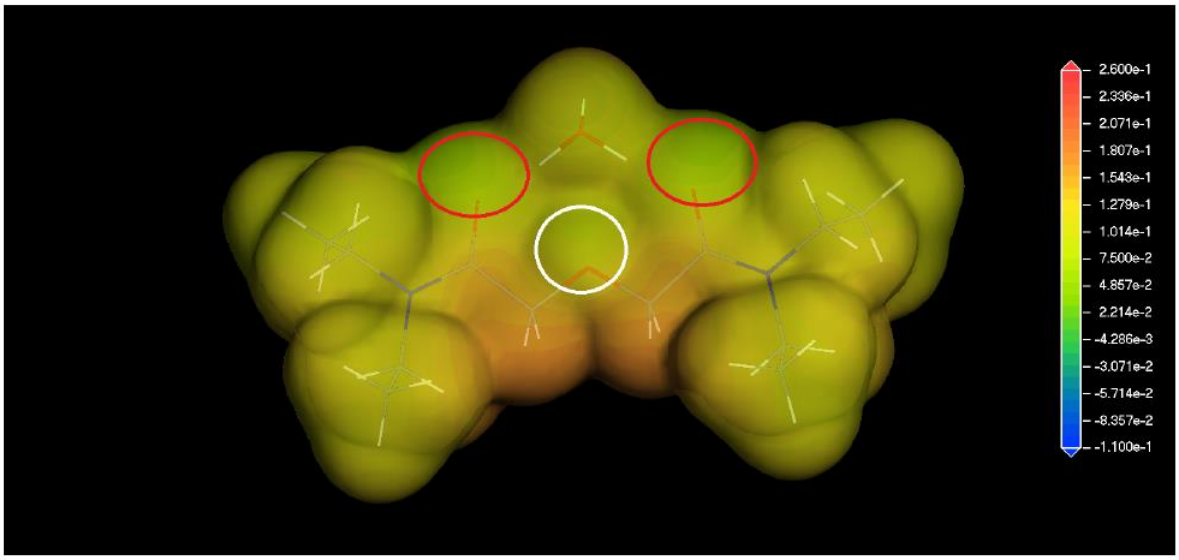

Figure 2.11 Electrostatic potential / H_3O^+ acid model calculated for TEDGA; ESP distribution mapped on 0.017 e/Å3 iso-surface of molecular electron density; red circles indicate the negative extremes at carbonyl oxygens, the white one then the minimum at ether oxygen. (DMol^3, DNP, B3LYP, GD2, COSMO)

2.1.7 BOND DISSOCIATION ENERGIES

Bond dissociation energies (BDE) are calculated as a sum of the energies of the two fragments resulting from cleaving a certain bond subtracted with the energy of the starting molecule. This gives an indication how much energy it takes at least to homolitically cleave the bond of interest. This kind of molecular property was

This project has received funding from the EURATOM research and training programme 2014-2018 under grant agreement No 755171. The content of this deliverable reflects only the author's view. The European Commission is not responsible for any use that may be made of the information it contains.

previously also calculated by Drader *et al.*[27] for *N,N*-dialkyl amides, where the results correlated with MS data for the behavior of the monoamides under irradiation.

First, different methods for the calculation of BDE are evaluated to make an efficient choice for the functional, optimizing computational resources. After confirmation of the method, the effect of methylation on the DGA backbone on the BDE is studied and compared to the previously published experimental findings. Additionally, the influence of the DGA alkyl chain length on the BDE of the C(2) N(1) bond is evaluated.

BENCHMARKING OF DFT FUNCTIONALS FOR BDE CALCULATIONS

This subsection is aimed on calculation of bond dissociation energies (BDE) of selected set of benchmarking molecules using different DFT functionals. The obtained results are compared to the experimental and computational findings published by Korth et al. [31] in order to determine whether or not a satisfactory results can be obtained with much faster standard DFT approach and if it is really needed to use more computationally demanding hybrid functionals (hybrid functionals require about 100 times more computing time).

The structures of the benchmarked molecules are shown in Figure 2.12. In Figure 2.13, experimental, published BDEs and calculated BDEs for breaking the C-H bond in ethyl methyl ether, acetic acid and methyl amine are shown.

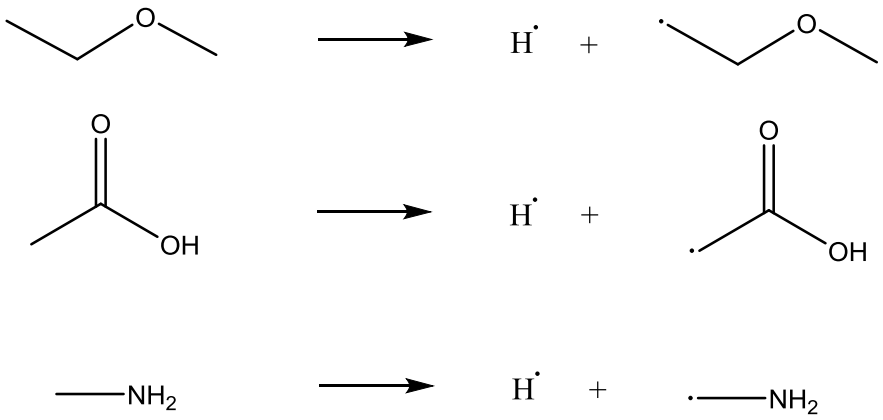

Figure 2.12 Start and end products for BDE calculations used for benchmarking

The experimental values and Hartree Fock (HF), second order Möller-Plesset (MP2) and Becke 3-Parameter Lee-Yang-Parr (B3LYP) [32-34] calculations were taken from Korth *et al*. [31]. At a first glance, it is clear that there are some significant deviations from the experimental values. Especially HF underestimates and Local-Density Approximation (LDA) overestimates bond strengths. What is most important from these results is that the order of the BDE values remains the same in all cases except for the combination of B88+SLA (i.e. accounting for the Becke exchange and no correlations, which should resemble HF results – such an approximation is thus not expected to perform well). For our purpose of qualitative evaluation of BDEs of different bonds, widely used PBE will be further on used in this Section in order to increase the efficiency of the use of computational resources.

This project has received funding from the EURATOM research and training programme 2014-2018 under grant agreement No 755171. The content of this deliverable reflects only the author's view. The European Commission is not responsible for any use that may be made of the information it contains.

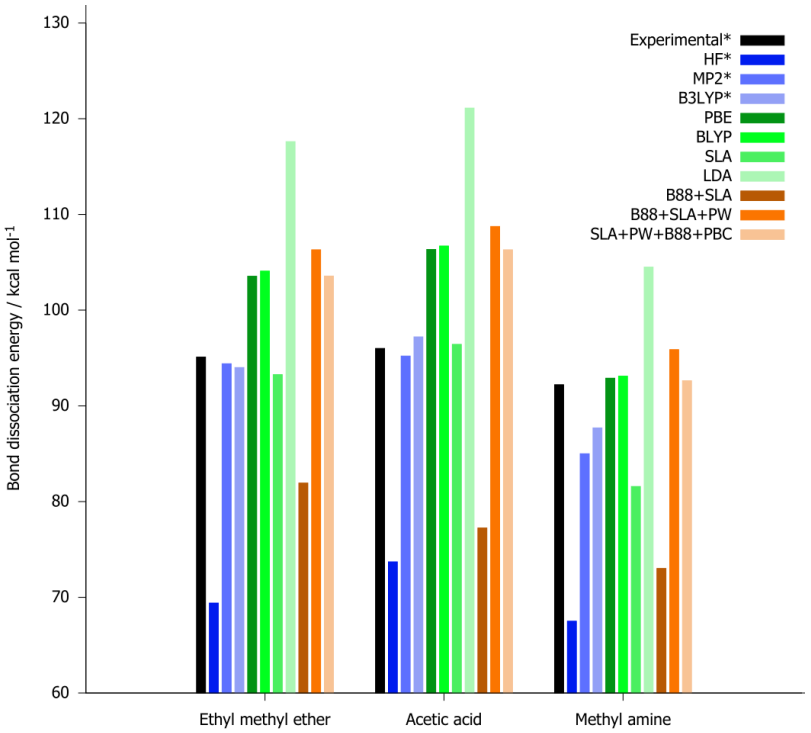

Figure 2.13 BDE of CH bond for three different organic molecules determined by different methods; experimental values, HF, MP2 and B3LYP calculations were taken from Korth *et al*. [31], these are marked in the legend with *

BOND DISSOCIATION ENERGIES OF METHYLATED TEDGA DERIVATES

In order to keep the computation time at a reasonable level, the calculations were conducted for the symmetric unsubstituted TEDGA derivative. In Figure 2.14, the calculated BDEs of TEDGA are shown for the bonds in the backbone of the structure. The bond which needs the lowest amount of energy to break is the C-O bond of the ether group. This is in agreement with the experimental irradiation studies, where products of breaking the ether bond were found most abundantly for TODGA radiolysis. [20-22]

When the backbone of TEDGA is methylated twice (Me_2-TEDGA), there are two different possibilities considering the stereochemistry. In one configuration, both methyl groups are oriented in the same direction (*RS*) in the other case the methyl groups are oriented to opposite sides of the backbone (*RR*). Interestingly, these seemingly small differences showed to greatly influence (up to two orders of magnitude) solvent extraction efficiency and change of selectivity for Me_2-TODGA. [35]

Methylation causes a decrease in BDE of the ether bond for both diastereomers (Figure 2.14). If a protective effect by methylation would occur, this could not be explained by the results above, although these calculations do not take steric effects into account. BDEs do not seem to be significantly different between the two diastereomers.

This project has received funding from the EURATOM research and training programme 2014-2018 under grant agreement No 755171. The content of this deliverable reflects only the author's view. The European Commission is not responsible for any use that may be made of the information it contains.

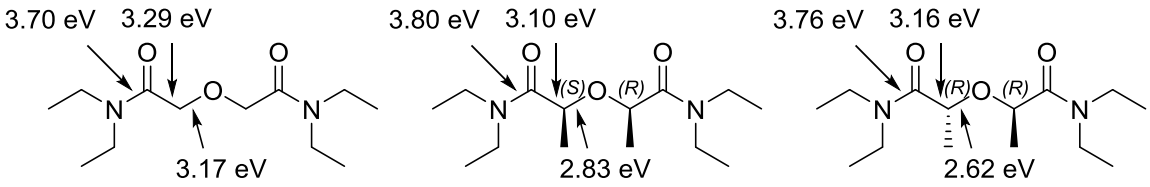

Figure 2.14 BDEs for TEDGA and two stereomers of Me_2-TEDGA

For methylation of the TODGA backbone, the extraction behavior follows the trend *D*(TODGA) > *D*(Me-TODGA) > *D*(Me_2-TODGA), [36] although, at high nitric acid concentrations, the extraction behavior of Me-TODGA resembles that of TODGA.[37] For the asymmetrical Me-TEDGA molecule, simulations show a decrease of the BDE of both ether bonds, not only for the methylated C-O bond (Figure 2.15) but also for the other C-O bond. This indicates that the introduction of a single methyl group into the DGA backbone weakens the molecule's structure. This simulation is in agreement with findings of Galán *et al*.[21] for Me-TODGA, where an increased degradation rate was observed for the single substituted variant, Me-TODGA, which was remarkable because it might be expected that the substitution with a methyl group could protect the molecule from radiolysis[1]. In experiments with short-chained TEDGA derivatives, there was no significant difference between the dose constants of Me-TEDGA and Me_2-TEDGA.[23] Contrary, in concentrated aqueous nitrate solution the dose constants become larger with methylation for TEDGA, Me-TEDGA and Me_2-TEDGA.[24]

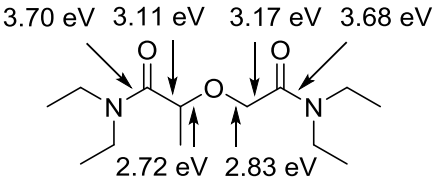

Figure 2.15 : BDEs for Me-TEDGA

INCREASING ALKYL CHAIN LENGTH OF DGAS

Since in experimental studies not only the degradation products of ether bond breaking were found, the breaking of the C-N bond between the amide and the alkyl groups was studied. For DGAs with short alkyl chains, there might be a significant difference expected in the BDE of these bonds. From Figure 2.16, it becomes clear that the biggest difference in the BDE occurs between the alkyl chains with a length of one and two carbon atoms. These results can be explained by the relative stability of methyl and ethyl radicals, which are the final products of homolytical cleavage of the C-N bond. Because the methyl radicals are much less stable than the ethyl radicals [38], the BDE is much lower for TEDGA than for TMDGA. This result seems to be in contrast with the observation that TMDGA degrades faster than TEDGA under gamma irradiation [23]. However, Horne *et al.* [24] showed experimentally that the degradation of hydrophilic DGA degradation is driven by $^{\bullet}OH$ and $^{\bullet}NO_3$ oxidation, of which the latter would become more important in concentrated HNO_3

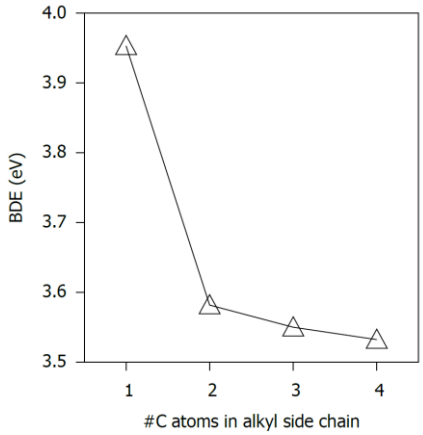

Figure 2.16 BDE of the C-N bond as a function of the length of the alkyl chains

[1]The apparent contradiction is tempered by the experimental observation that the prevailing decay products are linked to the unprotected C-O bond [22].

This project has received funding from the EURATOM research and training programme 2014-2018 under grant agreement No 755171. The content of this deliverable reflects only the author's view. The European Commission is not responsible for any use that may be made of the information it contains.

solutions because HNO_3 scavenges $^{\bullet}OH$ radicals. For this reason, the BDE of this C-N bond may not be very indicative for the degradation rate.

2.1.8 STABILITY INDICATORS DERIVED FROM MOLECULAR DYNAMICS

MOLECULAR STABILITY

Conformation states of the four different hydrophilic DGA derivatives (TMDGA, TEDGA, Me-TEDGA, Me2-TEDGA) dissolved in water have been also analyzed by application of statistical methods on the temporal trajectories obtained for canonical ensembles produced by means of classical molecular dynamics (MD) method.

The objective of the performed research was to test the influence of the real thermodynamic conditions (density, temperature) and the realistically represented solvent (water) molecular surroundings on the resulting dynamics and prevailing conformation states of the selected DGA derivatives in solution. It is likely that such mean conformation states will differ from the conformations predicted by QM ground state optimization, the difference possibly leading to modification of chemical stability indicators and the related bond stability predictions for the tested molecules. The dynamical behavior of the selected bonds that is extracted from the MD trajectories can provide additional information about energetic characteristics of the molecules (such as the bond rotation barrier) in a real solvent environment.

The simulations were performed within the Materials Studio (MS) simulation environment using the server modules MS Amorphous Cell and MS Forcite. Special SW tool written in the Matlab SW environment was developed in order to perform the detailed statistical analysis of the conformational dynamics. The forcefield MS COMPASS, Ewald evaluation of electrostatic interactions and atom-based summation of van der Waals interactions with the cut-off radius 1.6 nm was applied in all MD calculations

At first, the forcefields available in MS were tested on reliability of water simulations. 30 different initial instances were constructed using MS Amorphous cell containing 1110 water molecules in the one simulation cell (linked by periodic boundary condition with surrounding cells). Due to the restricted extend of the samples, the auto-ionization of water molecules was neglected. Each of the samples was let to evolve for 500 ps, and then the radial distribution functions g_{OO}, $g_{\bullet}$, g_{HH} and thermal capacity c_V has been calculated from the obtained trajectories and compared with the available experimental data. The best agreement has been achieved with the forcefield MS COMPASS, Ewald evaluation of electrostatic interactions and atom-based summation of van der Waals interactions; so, this settings were applied in all further calculations.

In the second step, samples were generated for each tested molecule using MS Amorphous Cell module. The samples contained 1110 water molecules per 1 ligand molecule placed in a cubic cell of dimensions conformal with the mass density 1 g/cm^3. In case of simulations involving acidic solutions, number of undissociated acid molecules corresponding to the desired molar concentration was added in the sample. The MD trajectories were then calculated under the following conditions: NVT dynamics, NHL thermostat, periodic boundary conditions, total simulation time 5 ns, time step 1 fs and temperature 293 K. One longer 40 ns simulation was also performed. Statistical reduction was applied in order to select the statistically inequivalent conformations. The threshold level was set to 1.5 ESD for each of the torsion angles shown in Figure 2.17.

This project has received funding from the EURATOM research and training programme 2014-2018 under grant agreement No 755171. The content of this deliverable reflects only the author's view. The European Commission is not responsible for any use that may be made of the information it contains.

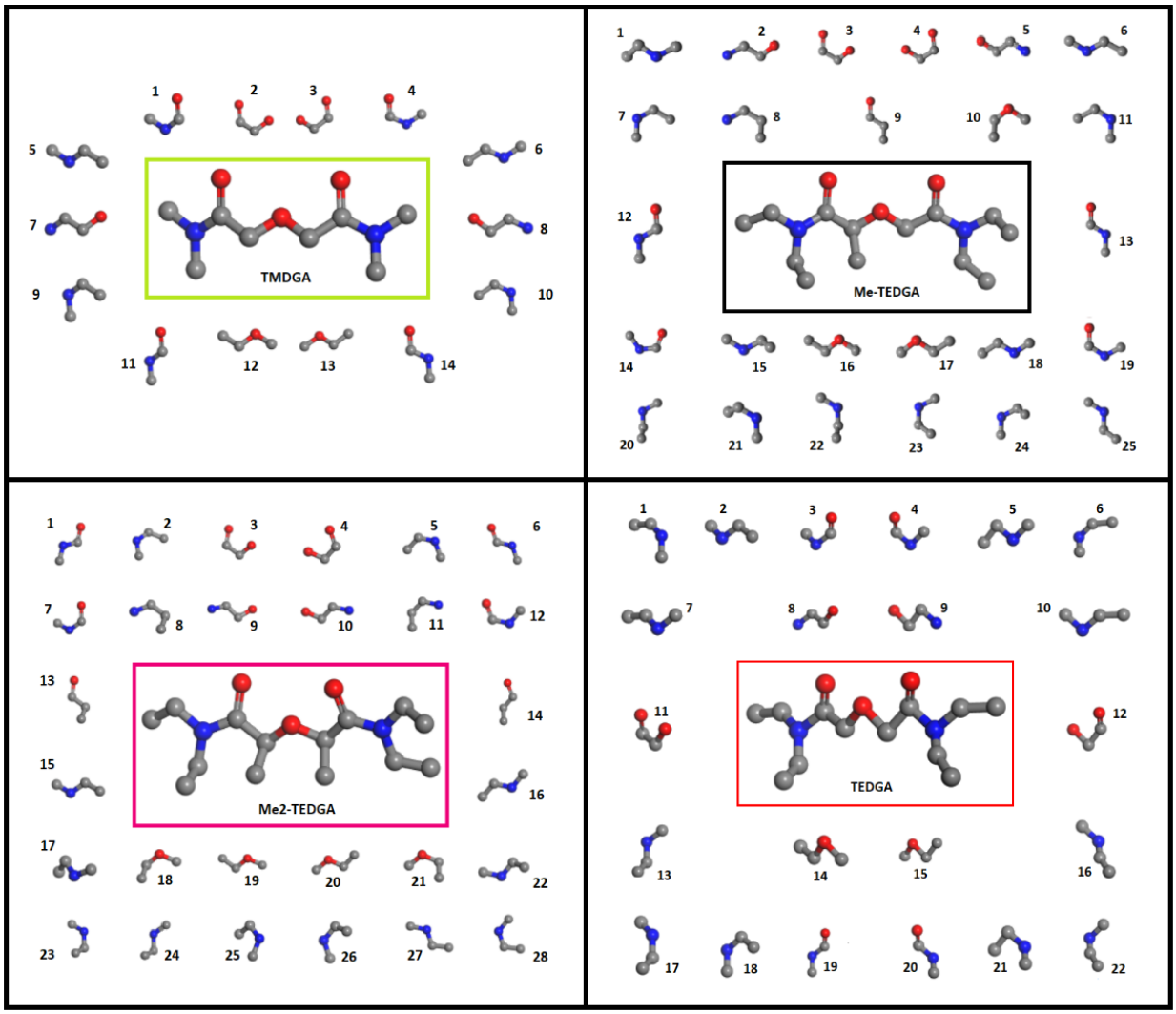

Figure 2.17 Torsion angles analyzed for the shown DGA derivatives

Number of distinguished conformation states obtained for TMDGA, TEDGA, Me-TEDGA and Me2-TEDGA amounts 4, 30, 24 and 64, respectively. The relatively high numbers provide evidence about the low energetic barriers restricting rotations around the available bonds, comparable with the thermal energy k_BT. During the simulations, the tested molecules "jumped" between the conformations in a random manner, independently on the simulation time.

The complex conformational analysis algorithm then provided, for each tested molecule and every torsion angle instance, a set of populated values together with the temporal frequency of their changes. Remarkable dependence (linked presumably to the influence of entropy) of the obtained distributions on the total simulation time is observed (Figure 2.18).

This project has received funding from the EURATOM research and training programme 2014-2018 under grant agreement No 755171. The content of this deliverable reflects only the author's view. The European Commission is not responsible for any use that may be made of the information it contains.

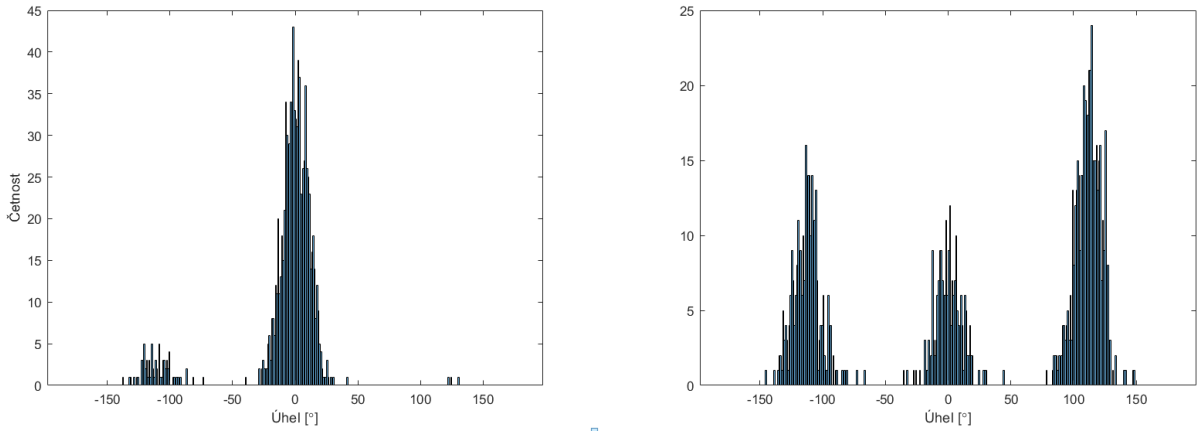

Figure 2.18 Example of the torsion angle distribution obtained from 5 ns simulation (picture on the left) and last 5 ns of 40 ns long simulation (right); equilibration in the observed conformational behavior is apparent.

In further analysis, normality of all the distributions is assumed. The number of Gaussian components is set to be equal to the number of maxima identified (by the proposed filtering algorithm) for the given torsion angle. From the Gaussian fits, the mean angular values of the given torsion angle are then obtained. A matrix describing conformational dynamics of the given molecule over the selected time interval is then calculated and analyzed in terms of two selected statistical parameters: the rate of conformational changes (L) and the total number of conformations (K) that appeared during the fixed testing time interval (5 ns).

Experimentally, it was found [23] that the radiation stability of the tested molecules in pure water decreases in the order Me_2-TEDGA ≈ Me-TEDGA > TEDGA > TMDGA that is in general inversely proportional to the molecular weight of the molecules. The calculated L-values are qualitatively very well correlated with the experimental order (Table 2.20), providing a significantly larger L-value for the less stable TMDGA, modestly larger for TEDGA, and smallest, nearly equal values for Me- and Me_2-TEDGA, in agreement with the nearly identical slopes of the concentration decay under irradiation [23]. Thus, following the observed correlation, a lower value of the indicator L suggests a higher stability of the molecule. Apparently, no such well-resolved correlation is found for the parameter K, where the value obtained for Me-TEDGA deviates from the expected trend.

Table 2.20 Parameters L and K (cf. the text) obtained for the tested molecules in pure water environment

parameter	TMDGA	TEDGA	Me-TEDGA	Me_2-TEDGA
L	766	370	310	315
K	157	178	131	203

Behavior of TEDGA was also experimentally tested in dependence on temperature and on the nitric and hydrochloride acids concentration in the irradiated solutions [24]. The radiolytic stability of TEDGA was found to decay with the both environmental parameters rising. Comparison of the mentioned experimental data with the values of parameters L and K obtained in simulations (Table 2.21) shows that both L and K copy well the trends of the experimental decay rates, including the initial stabilization effect of HNO_3 (cf. Table 2.20) as well as the observed rise of stability with the also tested growing HCl concentration. Comparison of the L-values obtained with TEDGA for pure water and aqueous nitric acid solutions provides, in this particular case, no support for possible stabilization through the acid presence predicted by experiment and QM calculations.

This project has received funding from the EURATOM research and training programme 2014-2018 under grant agreement No 755171. The content of this deliverable reflects only the author's view. The European Commission is not responsible for any use that may be made of the information it contains.

However, taking in account the proposed protective mechanism of nitric acid consisting in indirect radical screening, such finding is not surprising.

Table 2.21 Comparison of the calculated parameters L and K with the decay constants [h^{-1}] observed in [23] for TEDGA solutions at different temperature, HNO_3 and HCl concentrations

T [°C]	0,5 M HNO_3	L	K	4 M HNO_3	L	K	5 M HCl	L	K
25	$(1{,}1 \pm 0{,}1)\cdot10^{-3}$	459	245	$(1{,}2 \pm 0{,}2)\cdot10^{-3}$	515	283	$(7{,}0 \pm 0{,}4)\cdot10^{-2}$	756	499
45	$(8{,}5 \pm 0{,}1)\cdot10^{-3}$	640	342	$(8{,}8 \pm 0{,}5)\cdot10^{-3}$	659	317	8 M HCl		
65	$(5{,}0 \pm 0{,}6)\cdot10^{-2}$	737	478	$(7{,}8 \pm 0{,}6)\cdot10^{-2}$	809	463	$(5{,}2 \pm 0{,}2)\cdot10^{-2}$	707	432

BOND STABILITY

The results obtained from conformational analysis can also provide information about the dynamics of individual bonds that can be related to the stability of these bonds. We demonstrate such possibility on the following example.

In Ref. 24, products of the rupture of the C-O ether bond were identified for TEDGA, Me-TEDGA and Me_2-TEDGA, but not for TMDGA. Indeed, dynamics of the torsion angles related to the ether bond show high frequency changes in case of TEDGA, Me-TEDGA and Me_2-TEDGA (typical examples given in Figure 2.19), but a qualitatively different behavior is found for TMDGA (Figure 2.20), with one of the torsion angle involving the ether bond (marked as 12) “frozen” for a long time periods, resulting in a low-rate dynamics. The highest conformation change rate is then observed for the torsion angles involving the amide group (marked as ‘11’ and ‘14’ in Figure 2.20). With the proposed sense of the L-parameter in mind, such behavior might suggest a possibly different decay mechanism of TMDGA, involving primarily the amide groups instead of the ether group “preferred” in TEDGA and its derivatives.

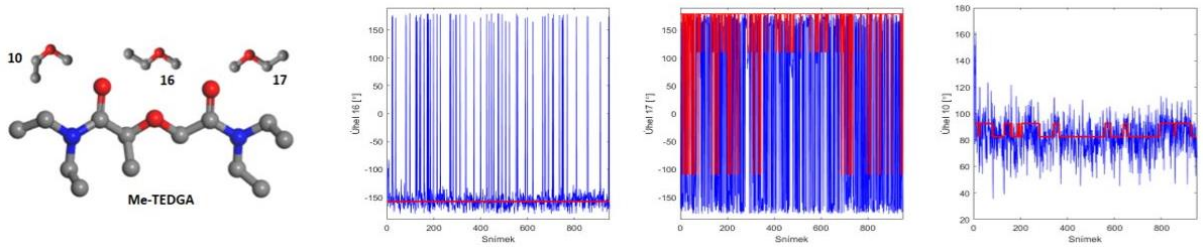

Figure 2.19 Me-TEDGA: the torsion angles involving the ether bond and the variation of these with the simulation time

This project has received funding from the EURATOM research and training programme 2014-2018 under grant agreement No 755171. The content of this deliverable reflects only the author’s view. The European Commission is not responsible for any use that may be made of the information it contains.

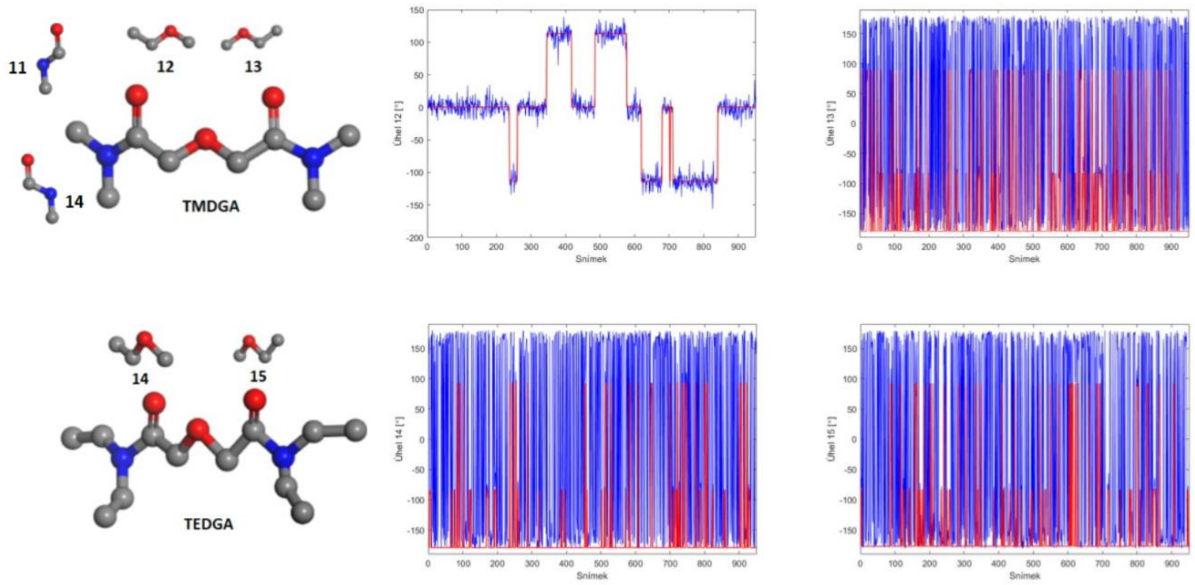

Figure 2.20 Torsion angles involving the ether bond in TMDGA (12, 13, upper row) and TEDGA (14, 15, lower row) followed by examples of their temporal dynamics. Notice the remarkably different course calculated for TMDGA

2.2 SIMULATION OF RADIOLYSIS REACTION PATHWAY

2.2.1 MECHANISMS BASED ON HYDROGEN ABSTRACTION

The degradation reaction pathways based on the hydrogen abstraction is investigated for the studied ligands TMDGA, TEDGA, Me-TEDGA and Me_2-TEDGA. No acid representation is considered during these calculations. In searching for transition states, the QST2, QST3 [39-40] and TS [41] algorithm options of Gaussian09 code (42] are used. Conformation analysis of reactants, intermediates and products is done by the CREST utility of xTB software.

Total energy of each compound is calculated separately with the thermochemistry correction taken into account and the final energies are normalized to the energy of reactants. The method used consists of the CC single point calculations in Orca software on geometries obtained by the DFT calculations with Def2TZVP basis set. The thermochemistry corrections from the DFT calculations are added to total energy obtained by the CC calculations. The applied approach is considered to be the best one available today and is used in all discussion within the Section 2.1.1.

The degradation mechanism considered here is initiated by a free radical, causing the abstraction of hydrogen atom bonded to one of the ether carbons (C(4), C(5)). The radical might be represented by a hydroxyl radical $^{\bullet}$OH (aqueous environment) or a hydrogen radical $^{\bullet}$H (lipophilic organic solution). Due to the abstraction, the ether C-O bond is supposed to break. Methyl groups added in methylated forms of TEDGA should protect the adjacent ether C-O bond. The respective set of considered reaction pathways for $^{\bullet}$OH and $^{\bullet}$H radical is shown in Figure 2.21 and Figure 2.22.

For the case of hydrogen abstraction caused by hydroxyl radical, the calculations of transition states appearing in the first step of reaction (Figure 2.21) did not converge to required saddle points. The reason for such behavior is unknown. Thus, only the results obtained for reactions initiated by hydrogen radical are presented and discussed below.

This project has received funding from the EURATOM research and training programme 2014-2018 under grant agreement No 755171. The content of this deliverable reflects only the author's view. The European Commission is not responsible for any use that may be made of the information it contains.

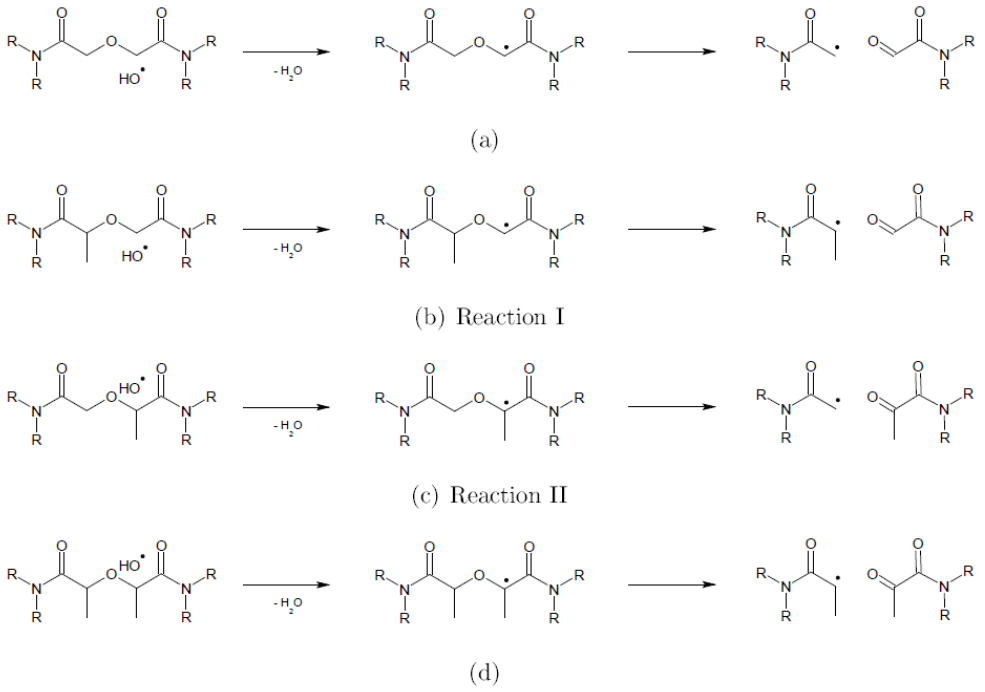

Figure 2.21 Reactions schemes considered for the degradation mechanism based on hydrogen abstraction initiated by attack of hydroxyl radical •OH on TMDGA and TEDGA (a), Me-TEDGA leading to rupture of the protected ether bond (b), Me-TEDGA causing a break of the unprotected ether bond (c) and Me_2-TEDGA (d)

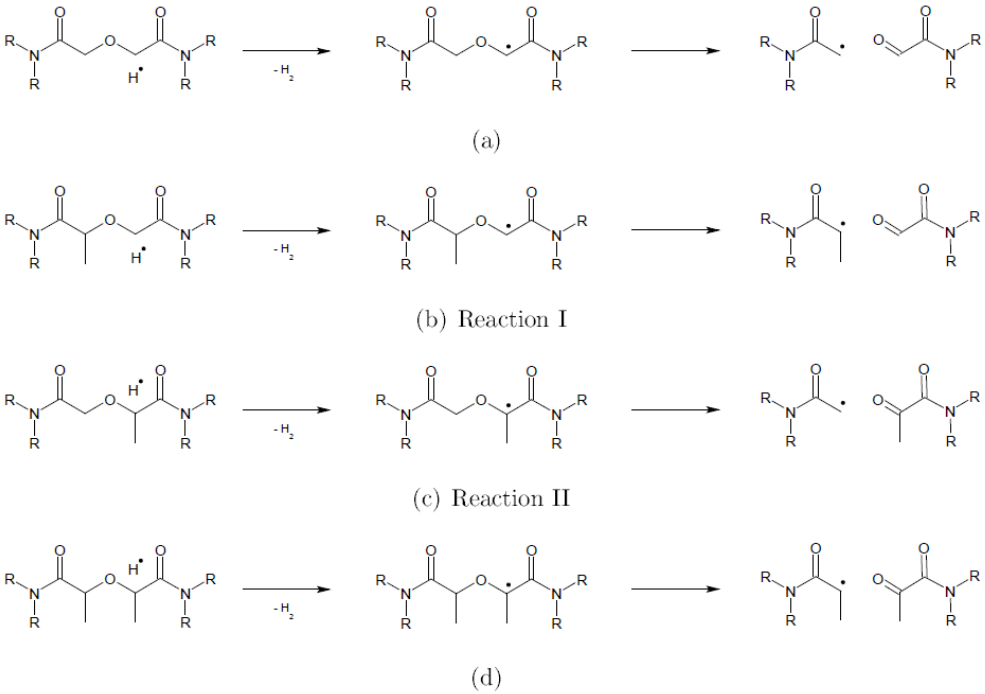

Figure 2.22 Reactions schemes considered for the degradation mechanism based on hydrogen abstraction initiated by attack of hydrogen radical •H on TMDGA and TEDGA (a), Me-TEDGA leading to rupture of the protected ether bond (b), Me-TEDGA causing a break of the unprotected ether bond (c) and Me_2-TEDGA (d)

This project has received funding from the EURATOM research and training programme 2014-2018 under grant agreement No 755171. The content of this deliverable reflects only the author's view. The European Commission is not responsible for any use that may be made of the information it contains.

Considering the abstraction of hydrogen adjacent to the ether group as the initiation of the subsequent degradation reaction, it must not be forgotten that in case of methylated TEDGA ligands, the number of possible reaction centers (number of hydrogen atoms adjacent to the ether group at positions R1 - R4) is reduced. TMDGA and TEDGA have four of these hydrogens, but only three hydrogens of this type are present in Me-TEDGA and only two hydrogens are in Me_2-TEDGA. This correspondingly reduces the overall probability of hydrogen abstraction for methylated ligands, in accordance with the experimentally observed trend of stability.

Energy diagrams obtained for the first reaction step and for the whole reaction pathway are shown in Figure 2.23 and 2.24, respectively. The energy profiles are summarized in Table 2.22. The corresponding values of activation energy and reaction energy are given in Table 2.23.

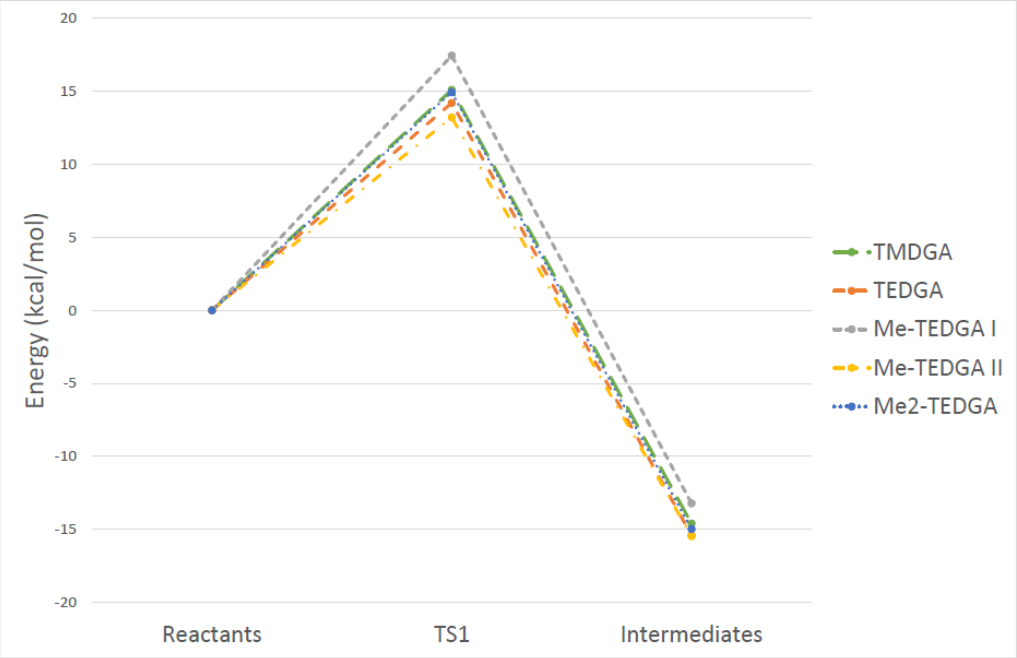

Figure 2.23 Energy profiles of the first step in the degradation mechanisms suggested in Figure 22 (Coupled Cluster Theory)

Table 2.22 Reaction energy (kcal /mol) of the individual steps in the degradation pathways shown in Figure 2.24; Coupled Cluster Theory, R stands for Reactants, TS1 for Transition state 1, I for intermediates, TS2 for Transition state 2 and P for Products.

molecule	R	TS1	I	TS2	P
TMDGA	0	15.08	-14.59	4.64	-17.35
TEDGA	0	14.19	-15.40	6.37	-17.69
Me-TEDGA Reaction I	0	17.43	-13.21	8.39	-19.93
Me-TEDGA Reaction II	0	13.20	-15.46	5.81	-23.00
Me_2-TEDGA	0	14.92	-14.97	5.94	-23.36

This project has received funding from the EURATOM research and training programme 2014-2018 under grant agreement No 755171. The content of this deliverable reflects only the author's view. The European Commission is not responsible for any use that may be made of the information it contains.

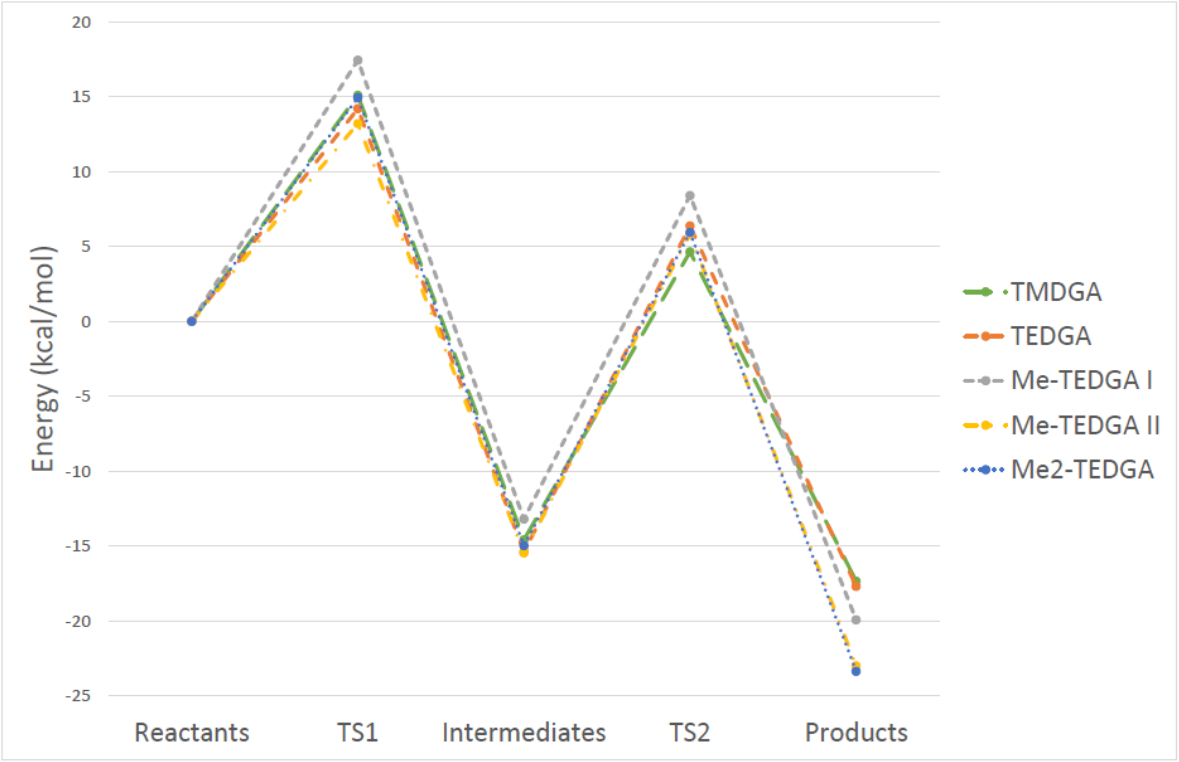

Figure 2.24 Energy profiles of the degradation mechanisms suggested in Figure 22 (Coupled Cluster Theory)

Table 2.23 Activation energy (Ea) and reaction energy (Er) of the proposed degradation pathway steps (cf. Figure 2.24) calculated with Coupled Cluster Theory; energy of each reaction step is listed separately

	First step		Second step	
molecule	**Ea (kcal/mol)**	**Er (kcal/mol)**	**Ea (kcal/mol)**	**Er (kcal/mol)**
TMDGA	15.08	-14.59	19.23	-2.76
TEDGA	14.19	-15.40	21.76	-2.30
Me-TEDGA Reaction I	17.43	-13.21	21.60	-6.73
Me-TEDGA Reaction II	13.20	-15.46	21.27	-7.53
Me_2-TEDGA	14.92	-14.97	20.90	-8.39

The activation energy (Ea) of the first reaction step (Figure 2.23) are similar for all ligands, with exception of Me-TEDGA / reaction I option, where the highest energy barrier of 17.43 kcal/mol is observed, in contrast to 13.20 kcal/mol for the reaction II option. The same observation was made for the methylated derivative of TODGA (TWE 21) [25]. The activation energy for TMDGA (15.08 kcal/mol) is higher than for TEDGA (14:19 kcal/mol). This behavior contradicts the experimentally observed stability [23-24]. However, it is in agreement with the experimental rate coefficients for this reaction measured in [24] ($1.22\pm0.03 \times 10^8$ $mol^{-1}s^{-1}$ for TMDGA and $1.60\pm0.03 \times 10^8$ $mol^{-1}s^{-1}$ for TEDGA). The activation energy for Me_2-TEDGA is 14.92 kcal/mol that is higher than for TEDGA but lower than for TMDGA. The latter relation contradicts the experimentally measured rate coefficient for Me_2-TEDGA ($0.36\pm0.07 \times 10^8$ $mol^{-1}s^{-1}$ [24]). However, the energy difference between TMDGA and Me_2-TEDGA is small. In such case, caution is advised when interpreting such small energetic differences because the influence of uncertainties and fluctuations in the geometries of the transient states can be significant [25].

This project has received funding from the EURATOM research and training programme 2014-2018 under grant agreement No 755171. The content of this deliverable reflects only the author's view. The European Commission is not responsible for any use that may be made of the information it contains.

Difference in the calculated activation energy of the second reaction step is very small for all studied ligands, preventing us from making any definite conclusions or comparison. Apparently, the activation barriers of the second reaction step overweight these of the first reaction step for all tested ligands (Table 2.23). This suggests that the second reaction step determines the overall reaction rate. A similar and even more remarkable inbalance in the activation energies of the first and second reaction step was already simulated by DFT for TODGA and its methylated derivatives [25]. The here reported values obtained by much more reliable Coupled Cluster Theory confirm this phenomenon.

In study of TODGA and its methylated derivatives [25], thermodynamic control of the reaction was suggested to be dominant. In such case, the change in potential energy between the reactants and the products would have a decisive impact on the composition of final products [25]. The conclusion stem from comparison of the activation energy and high reaction energy observed for the first reaction step. However, the latter is not the case for the hydrophilic DGAligands studied here (cf. Table 2.23).

Furthermore, for the second reaction step, the reaction energy is much lower than the activation energy for all ligands (cf. Figure 2.24) and the relative size of the total potential energy drop calculated for individual ligands is in disagreement with the experimentally observed stability relation of the ligands (TMDGA < TEDGA < Me-TEDGA ≤ Me_2-TEDGA [23]).

In the particular case of Me-TEDGA, the energetic parameters calculated for the first reaction step seems to sligtly prioritize the reaction II. In the second reaction step, the activation and reaction energies are almost the same for both possible reactions (Ea = 21.60 kcal/mol for reaction I and 21.27 kcal/mol for reaction II; Er = 6.73 kcal/mol for reaction I and 7.53 kcal/mol for reaction II), and the mutual comparison is again in favor of the more likely rupture of the non-protected C-O ether bond. Nevertheless, caution must be taken when interpreting such small energetic differences.

Let's finally notice that In the case of hydrogen abstraction initiated by a hydroxyl radical, only the activation energy of the first reaction step would be different. The rest of the proposed reaction is the same as for the hydrogen radical. The experimental studies [23-24] suggest that role of the hydroxyl radical is dominant. Unfortunately, corresponding transition states were not found.

2.2.2 ALTERNATIVE REACTION PATHWAY

Similar to the previous Section, evaluation of the energetics of the degradation routes is based [25] on calculation of Gibbs free energy change $\Delta G = \Delta H - T \times \Delta S$. The entropy contribution to the free energy is usually effectivelly neglected (T = 0) or approximated with the ideal gas phase expression for vibrational (Sv), translational (St) and rotational (Sr) parts. The solvent effects, that may be significant, are not accounted for.

Further on, the solvation entropy model published recently by Garza [43] is implemented for reaction path calculations. These results are compared to the published experimental findings and simulations. It is shown that the influence of the solvent entropy can have major consequences for the value of the ΔG for a certain reaction step. Certainly, entropy effects drive the reaction if there are more end products and significant entropy changes occur.

In the context of radiolysis research, often the reaction pathway between the original and the final compounds remain a question because the intermediate products are often of a radical nature and consequentially short-lived species. In the literature, a reaction pathway was suggested by Koubský *et al.*[25] for DGAs. It starts with hydrogen abstraction on one of the methylene groups next to the ether oxygen. This reaction pathway is

This project has received funding from the EURATOM research and training programme 2014-2018 under grant agreement No 755171. The content of this deliverable reflects only the author's view. The European Commission is not responsible for any use that may be made of the information it contains.

shown in Figure 2.25, together with the Gibbs free energies calculated in two different ways. The Gibbs free energies for which ΔS was approximated based on ideal gas formulas insinuate that ΔG decreases in both reaction steps, so that the final products are thermodynamically favorable. However, when solvent corrections (*n*-dodecane) are incorporated for ΔS, the second reaction step does not result in a decrease in ΔG. For the DFT energy, solvent interactions were calculated using ENVIRON. Approximation of ΔS in the solvent was obtained by the mentioned method of Garza. Van der Waals volumes, which are input parameters for this approach, were calculated as published by Bondi[44]. The results of implementing this solvent model suggests that, when applying more realistic simulation conditions, this reaction path would not be energetically advantageous. This is in agreement with experimental data, where the product of the reaction shown in Figure 2.25 is not observed or only in small amounts.

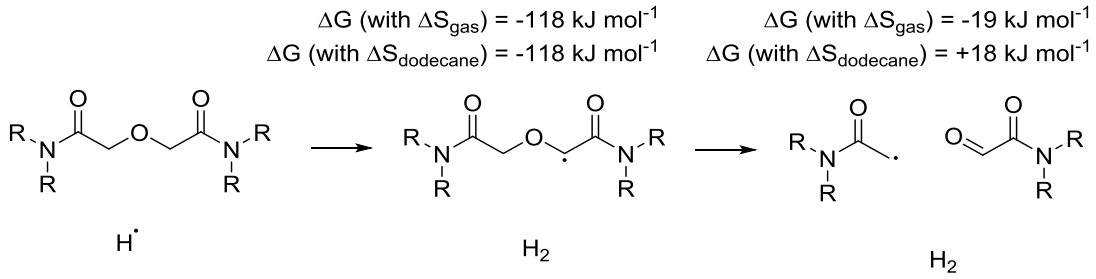

Figure 2.25 Calculated changes in Gibbs free energy for the suggested hydrogen abstraction mechanism

Different experimental irradiation experiments show that products of ether bond breaking are the main degradation products of DGA degradation. For this reason, Gibbs free energies were calculated between begin and end products of the reaction resulting in one of the most significant experimentally observed degradation compounds (with the alcohol group) [18, 22, 23, 45]. The result of this calculation is shown in Figure 2.26. This strongly negative value for ΔG suggests that this reaction is energetically much more favorable. The reaction mechanism with activation energies in between reaction steps could be considered as well, however the current calculations already give a clear indications about thermodynamics.

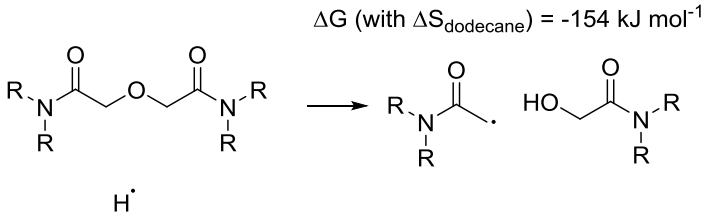

Figure 2.26 Calculated Gibbs free energies for the reaction leading to an observed degradation compound.

This project has received funding from the EURATOM research and training programme 2014-2018 under grant agreement No 755171. The content of this deliverable reflects only the author's view. The European Commission is not responsible for any use that may be made of the information it contains.

CONCLUSIONS

An extensive set of simulation results has been collected and analyzed related to stability descriptors and radiation decay routes of two types of extraction agents, CyMe4-BTBP and DGA derivatives. Overview of the results and their detail analysis and discussion is given in Section 1 and Section 2 of the Deliverable. Based on analysis of these complex results, the following conclusions deserve to be highlighted.

- For $CyMe_4$-BTBP, the radiolysis degradation pathway in 1-octanol solvent is proposed, resulting in $CyMe_4$-BTBP – octanol adduct conformal with the experimental observations, and the energetically most favorable structures and reaction route is identified.
- In case of DGAs, the obtained results mainly relate to hydrophilic derivatives - TMDGA, TEDGA, Me-TEDGA and Me_2-TEDGA – studied within a pure water environment as well as in an acidic solution simulated by three different acid representation: H^+, H_3O^+ and HNO_3 models.
  - Creation of hydrogen bonds is anticipated for all studied hydrophilic DGAs in frame of H^+ acid model, and for TEDGA also within the HNO_3 model.
  - Calculated radical Fukui functions show, for all the tested hydrophilic DGAs, the trend that is in concert with the experimental stability studies. The same trend is then preserved with the acid models included. The observed maxima of the function are localized in vicinity of the ether hydrogens and the amide groups. This localization remains valid also for the calculated radical Fukui charges.
  - In case of TMDGA, the probability of hydrogen abstraction from the ether group indicated by the high radical Fukui charges on ether hydrogens is found to be comparable to the hydrogen abstraction from any of the CH_3 groups, in contrast to the rest of tested DGAs; similar situation is observed for the H^+ acid model.
  - Inclusion of acid influence leads to reduction of the radical Fukui charges mainly on the ether group, and does not significantly change the basic stability trends observed with no acid present; in case of the H^+ acid model, the difference among the ligands is even deepened.
  - The radial Fukui function distributions calculated for hydrophilic DGAs, TODGA and mTDDGA show similar localization of the main maxima, suggesting a similar susceptibility to radical attack for the different DGA ligands.
  - The electrophilic Fukui charges suggest a key role of the amide carbon C(2) in possible stabilization of the TEDGA and its derivatives against electrophilic attack on the amide group and confirm a different character of TMDGA comparing the TEDGA-based compounds.
  - Similar electrophilic reactivity of all hydrogen atoms is predicted by calculated values of electrophilic Fukui charges for all tested DGAs molecules, both in the acid-free situation and with any of the tested acid models included.
  - The HOMO-LUMO gap energy, partial atomic charges, bond orders and electrostatic potential distributions calculated for the tested models provide no simple guidance in respect to the resulting stability predictions.
  - The calculated BDEs show that methylation of the DGA backbone can decrease the amount of energy necessary to homolytically cleave the ether bonds in certain cases.
  - A new type of descriptor based on molecular dynamics simulations and subsequent statistical analysis of the obtained trajectories has been proposed and its relevance for the studied hydrophilic DGA derivatives successfully tested on molecular level as well as on level of individual bonds.

This project has received funding from the EURATOM research and training programme 2014-2018 under grant agreement No 755171. The content of this deliverable reflects only the author's view. The European Commission is not responsible for any use that may be made of the information it contains.

- Radiolysis reaction routes initiated by hydrogen radical and including hydrogen abstraction are simulated including the transition states, and the values of activation and reaction energy obtained for all studied hydrophilic DGAs. Only small energetic differences are found between the individual derivatives, with the activation and reaction energies of the same order for both reaction steps considered.
- In context of the simulation of reaction paths, the solvent effect is discussed. Namely, inclusion of solvent entropy is tested and found to change the estimated reaction Gibbs free energy in the way favoring the reaction route conformal with the experimental data. However, the role of solvent can be strongly influenced by the particular radical reaction type [85]. Thus, importance of the solvent entropy as a decision-making factor for selection of a certain reaction pathway will be further investigated.

- The simulation works provided also results related to practical performance and feasibility of applied methods.
  - Results of calculations of the BDE of the C-H bonds in ethyl methyl ether, acetic acid and methyl amine with different calculations methods are used to show that in most cases the order of calculated BDE values does not change compared to the experimental values. By choosing to use the PBE functional, computational resources can be kept reasonably low, even when increasing the size of the studied molecular system. This finding might be of practical importance when expansion of the studied model is desirable. However, the resulting tradeoff between the reduction of computing costs and loss of theoretical precision of the results obtained for larger molecular systems should be further carefully analyzed.
  - Set of reliable, standard simulation methods / settings / tools used to conformation analysis, geometrical optimization, transient state search and calculation of individual descriptors has been consolidated. Coupled Cluster Theory has been successfully applied to calculations of single point energies of the reactants, reaction intermediates and products, and proofed to provide very reliable and stable results.
- Analysis of the results obtained with the molecular stability descriptors derived from ab-initio quantum mechanical calculations and molecular dynamics simulations suggests a promising direction for further improvement, based on a proper merging of the two approaches.

This project has received funding from the EURATOM research and training programme 2014-2018 under grant agreement No 755171. The content of this deliverable reflects only the author's view. The European Commission is not responsible for any use that may be made of the information it contains.

APPENDIX – METHODS AND COMPUTATIONAL SETTINGS

The calculations results referred in Sections 2.1.7, 2.2.7 and shown in Figure 2.9 were conducted with DFT Quantum Espresso package [46] using the Jülich Aachen Research Alliance High Performance Computing (JARA-HPC) partition on the Rheinisch-Westfälische Technische Hochschule (RWTH) cluster. Calculations were conducted in vacuum with the Perdew-Burke-Ernzerhof (PBE) functional.[47] The effect of solvent has been computed assuming continuum solvation model with ENVIRON package, using the dielectric constant of *n*-dodecane of 2.0.[48] Initial structures were created in ChemDraw version 14.0, with initial geometry optimization performed with the aid of molecular mechanics.

All other DFT calculation were done by DMol^3 and Gaussian09 programs. The CC calculations were performed by Orca code. The geometry optimization started with generated initial geometries in the Gaussian09 program [42] with the following settings: 6-31G(d,p) basis set [49-50], PCM solvent model [51-53] with water as a solvent, GD3BJ dispersion correction [54-55] and B3LYP exchange and correlation functional [33].

Conformation analysis for reaction calculations was done with CREST utility [56] of xTB Semi-empirical Extended Tight-Binding Program Package [57-59]. This software generates the thermally accessible ensemble of minimum-energy structures generally consisting of conformers as well as rotamers using combination of Molecular Dynamic and Tight-Biding approximation [60]. Further optimization was performed on the conformations with the lowest energy gained by the CREST utility of xTB with the following settings: 6-311G++(2d,d,p) [61-62] and Def2TZVP [63-64] basis sets, PCM solvent model [51-53] with water as a solvent, GD3BJ dispersion correction [51-52] (section 1.2.4) and B3LYP exchange and correlation functional [33].

Gaussian09 code [42] was used for the geometric optimization and HOMO/LUMO calculations. Wiberg bond indices and Natural population analysis were calculated with Gaussian09 in combination with NBO 6.0 software [65] with the following settings: 6-31G(d,p) basis set [49-50], PCM solvent model [51-53] with water as a solvent, GD3BJ dispersion correction [54-55] (section 1.2.4) and B3LYP exchange and correlation functional [33]. Gaussian09 code was also used for searching transition states of the degradation reaction mechanism initiated by the hydrogen abstraction (section 2.1.1) using QST2, QST3 [39, 40] and TS [41] algorithm selections. The following settings was used for searching the transition states: 6-311++G(2d,d,p) [61-62] and Def2TZVP [63-64] basis sets, PCM solvent model [51-53] with water as a solvent, GD3BJ dispersion correction [51-52] and B3LYP exchange and correlation functional [33]. Furthermore, energy of reactants, intermediates and products were determined by Gaussian09 code with above mentioned settings with thermochemistry implemented in Gaussian09 code [66].

CC calculations [67-73] were done by Orca software [74-75] for single-point calculations of energy of reactants, transition states, intermediates and products on the geometries gained by DFT calculations using Gaussian09. Following settings were used: DLPNO-CCSD(T) level of theory, Def2TZVP [63-64] basis set and RIJCOSX approximation (RI-J for Coulomb integrals and COSX numerical integration for HF exchange) [76-78]. Thermochemistry corrections are added from the Gaussian09 DFT calculations.

Material studio DMol^3 [79-80] module was used to determine the subsequent properties of the electronic structure relevant for the stability study. These attributes are Fukui functions, Fukui charges, Mulliken population analysis, Hirshfeld population analysis, partial charges fitted from the electrostatic potential, bond orders based on Mulliken and Mayer theory and the electrostatic potential with the following settings: DNP basis set [79], COSMO solvent model [81-82], GD2 dispersion correction [83-84] and B3LYP correlation functional [33].

This project has received funding from the EURATOM research and training programme 2014-2018 under grant agreement No 755171. The content of this deliverable reflects only the author's view. The European Commission is not responsible for any use that may be made of the information it contains.

Molecular dynamics calculations used in Section 2.1.8 were performed within the Materials Studio (MS) simulation environment using the server modules MS Amorphous Cell and MS Forcite. Special SW tool written in the Matlab SW environment was developed in order to perform the detailed statistical analysis of the conformational dynamics. The forcefield MS COMPASS, Ewald evaluation of electrostatic interactions and atom-based summation of van der Waals interactions with the cut-off radius 1.6 nm, NVT dynamics, NHL thermostat, periodic boundary conditions, total simulation time 5 ns, time step 1 fs and temperature 293 K was applied in all MD calculations.

REFERENCES

1 Schmidt, H.; Wilden, A.; Modolo, G.; Bosbach, D.; Santiago-Schűbel, B.; Hupert, M.; Švehla, M.; Grűner, B.; Ekberg, C. Gamma radiolysis of the highly selective ligands CyMe4-BTBP and CyMe4-BTPhen: Qualitative and quantitative investigation of radiolysis products. Procedia Chemistry 21 (2016) 32 – 37.

2 Joule, J. .A.; Mills, K. Pyridines: Reactions and synthesis. In Heterocyclic chemistry, Fifth edition, chapter 8, pages 125-141. John Wiley Sons, Chichester UK, 2010.

3 Freeman, G. R. The radiolysis of alcohols. In: Actions Chimiques et Biologiques des Radiation, M. Haissinski (ed.) 14 (1970) 73-134.

4 Modolo, G.; Wilden, A.; Geist, A.; Magnusson, D.; Malmbeck, R. A review of the demonstration of innovative solvent extraction processes for the recovery of trivalent minor actinides from PUREX raffinate. *Radiochim. Acta* 2012, *100*, 8-9, 715-725. DOI:10.1524/ract.2012.1962.

5 Modolo, G.; Geist, A.; Miguirditchian, M. Minor actinide separations in the reprocessing of spent nuclear fuels: recent advances in Europe. Chap. 10 In *Reprocessing and Recycling of Spent Nuclear Fuel*; Taylor, R., Ed.; Woodhead Publishing: Oxford, 2015; 245-287.

6 Sasaki, Y.; Sugo, Y.; Suzuki, S.; Tachimori, S. The Novel Extractants, Diglycolamides, for the Extraction of Lanthanides and Actinides in HNO_3-*n*-dodecane System. *Solvent Extr. Ion Exch.* 2001, *19*, 1, 91-103. DOI:10.1081/SEI-100001376.

7 Bell, K.; Carpentier, C.; Carrott, M.; Geist, A.; Gregson, C.; Hérès, X.; Magnusson, D.; Malmbeck, R.; McLachlan, F.; Modolo, G.; Müllich, U.; Sypula, M.; Taylor, R.; Wilden, A. Progress Towards the Development of a New GANEX Process. *Proc. Chem.* 2012, *7*, 392-397. DOI:10.1016/j.proche.2012.10.061.

8 Carrott, M.; Bell, K.; Brown, J.; Geist, A.; Gregson, C.; Hères, X.; Maher, C.; Malmbeck, R.; Mason, C.; Modolo, G.; Müllich, U.; Sarsfield, M.; Wilden, A.; Taylor, R. Development of a New Flowsheet for Co-Separating the Transuranic Actinides: The “EURO-GANEX” Process. *Solvent Extr. Ion Exch.* 2014, *32*, 5, 447-467. DOI:10.1080/07366299.2014.896580.

9 Malmbeck, R.; Magnusson, D.; Bourg, S.; Carrott, M.; Geist, A.; Hérès, X.; Miguirditchian, M.; Modolo, G.; Müllich, U.; Sorel, C.; Taylor, R.; Wilden, A. Homogenous Recycling of Transuranium Elements from Irradiated Fast Reactor Fuel by the EURO-GANEX Solvent Extraction Process. *Radiochim. Acta* 2019, *107*, 9-11, 917-929. DOI:10.1515/ract-2018-3089.

10 Wilden, A.; Schreinemachers, C.; Sypula, M.; Modolo, G. Direct Selective Extraction of Actinides (III) from PUREX Raffinate using a Mixture of $CyMe_4$BTBP and TODGA as 1-cycle SANEX Solvent. *Solvent Extr. Ion Exch.* 2011, *29*, 2, 190-212. DOI:10.1080/07366299.2011.539122.

11 Modolo, G.; Wilden, A.; Daniels, H.; Geist, A.; Magnusson, D.; Malmbeck, R. Development and Demonstration of a new SANEX Partitioning Process for Selective Actinide(III)/Lanthanide(III) Separation

This project has received funding from the EURATOM research and training programme 2014-2018 under grant agreement No 755171. The content of this deliverable reflects only the author’s view. The European Commission is not responsible for any use that may be made of the information it contains.

using a mixture of $CyMe_4BTBP$ and TODGA. *Radiochim. Acta* 2013, *101*, 3, 155-162. DOI:10.1524/ract.2013.2016.

12 Modolo, G.; Wilden, A.; Kaufholz, P.; Bosbach, D.; Geist, A. Development and demonstration of innovative partitioning processes (i-SANEX and 1-cycle SANEX) for actinide partitioning. *Progr. Nucl. Energ.* 2014, *72*, 107-114. DOI:10.1016/j.pnucene.2013.07.021.

13 Wilden, A.; Modolo, G.; Kaufholz, P.; Sadowski, F.; Lange, S.; Sypula, M.; Magnusson, D.; Müllich, U.; Geist, A.; Bosbach, D. Laboratory-Scale Counter-Current Centrifugal Contactor Demonstration of an Innovative-SANEX Process Using a Water Soluble BTP. *Solvent Extr. Ion Exch.* 2015, *33*, 2, 91-108. DOI:10.1080/07366299.2014.952532.

14 Sasaki, Y.; Suzuki, H.; Sugo, Y.; Kimura, T.; Choppin, G. R.. New watersoluble organic ligands for actinide cations complexation. Chemistry Letters, 35(3):256-257, 2006. DOI 10.1246/cl.2006.256.

15 Rostaing, C.; Poinssot, C.; Warin, D.; Baron, P.; Lorraina, B. Development and validation of the EXAm separation process for single Am recycling. Procedia Chemistry, 7:367-373, 2012.

16 Lumetta, G. V.; Gelis, A. V.; Carter, J. C.; Niver, C. M.; Smoot, M. R. The actinide-lanthanide separation concept. Solvent Extraction and Ion Exchange, 32(4):333-347, 2014.

17 Van Hecke, K.; Modolo, G. Separation of actinides from low level liquid wastes (LLLW) by extraction chromatography using novel DMDOHEMA and TODGA impregnated resins. Journal of radioanalytical and nuclear chemistry, 261(2):269-275, 2004.

18 Sugo, Y.; Sasaki, Y.; Tachimori, S. Studies on Hydrolysis and Radiolysis of *N*,*N*,*N*′,*N*′-tetraoctyl-3-oxapentane-1,5-diamide. *Radiochim. Acta* 2002, *90*, 3, 161-165.

19 Sugo, Y.; Izumi, Y.; Yoshida, Y.; Nishijima, S.; Sasaki, Y.; Kimura, T.; Sekine, T.; Kudo, H. Influence of Diluent on Radiolysis of Amides in Organic Solution. *Radiat. Phys. Chem.* 2007, *76*, 5, 794-800. DOI:10.1016/j.radphyschem.2006.05.008.

20 Zarzana, C. A.; Groenewold, G. S.; Mincher, B. J.; Mezyk, S. P.; Wilden, A.; Schmidt, H.; Modolo, G.; Wishart, J. F.; Cook, A. R. A Comparison of the γ-Radiolysis of TODGA and T(EH)DGA Using UHPLC-ESI-MS Analysis. *Solvent Extr. Ion Exch.* 2015, *33*, 5, 431-447. DOI:10.1080/07366299.2015.1012885.

21 Galán, H.; Zarzana, C. A.; Wilden, A.; Núñez, A.; Schmidt, H.; Egberink, R. J. M.; Leoncini, A.; Cobos, J.; Verboom, W.; Modolo, G.; Groenewold, G. S.; Mincher, B. J. Gamma-Radiolytic Stability of New Methylated TODGA Derivatives for Minor Actinide Recycling. *Dalton Trans.* 2015, *44*, 41, 18049-18056. DOI:10.1039/c5dt02484f

22 Hubscher-Bruder, V.; Mogilireddy, V.; Michel, S.; Leoncini, A.; Huskens, J.; Verboom, W.; Galán, H.; Núñez, A.; Cobos Sabate, J.; Modolo, G.; Wilden, A.; Schmidt, H.; Charbonnel, M.-C.; Guilbaud, P.; Boubals, N. Behaviour of the Extractant Me-TODGA Upon Gamma Irradiation: Quantification of the Degradation Compounds and Individual Influences on Complexation and Extraction. *New J. Chem.* 2017, *41*, 13700-13711. DOI:10.1039/C7NJ02136D.

23 Wilden, A.; Mincher, B. J.; Mezyk, S. P.; Twight, L.; Rosciolo-Johnson, K. M.; Zarzana, C. A.; Case, M. E.; Hupert, M.; Stärk, A.; Modolo, G. Radiolytic and Hydrolytic Degradation of the Hydrophilic Diglycolamides. *Solvent Extr. Ion Exch.* 2018, *36*, 4, 347-359. DOI:10.1080/07366299.2018.1495384

24 Horne, G. P.; Wilden, A.; Mezyk, S. P.; Twight, L.; Hupert, M.; Stärk, A.; Verboom, W.; Mincher, B. J.; Modolo, G. Gamma Radiolysis of Hydrophilic Diglycolamide Ligands in Concentrated Aqueous Nitrate Solution. *Dalton Trans.* 2019, *48*, 17005–17013. DOI:10.1039/C9DT03918J.

This project has received funding from the EURATOM research and training programme 2014-2018 under grant agreement No 755171. The content of this deliverable reflects only the author's view. The European Commission is not responsible for any use that may be made of the information it contains.

25 Koubský, T.; Fojtíková, J.; Kalvoda, L. Radical degradation stability of ether linkage in *N,N,N',N'*-tetraoctyldiglycolamide and related organic extractants: A density functional study. *Prog. Nucl. Energ.* 2017, *94*, 208-215. DOI:10.1016/j.pnucene.2016.07.010.

26 Koubsky, T.; Lustinec, J. Application of quantum mechanical simulations for studying the radiolytic stability of prospective extractants in the nuclear fuel cycle. *J. Radioanal. Nucl. Chem.* 2018, *318*, 3, 2407-2413. DOI:10.1007/s10967-018-6225-2.

27 Drader, J. A.; Boubals, N.; Cames, B.; Guillaumont, D.; Guilbaud, P.; Saint-Louis, G.; Berthon, L. Radiolytic stability of *N,N*-dialkyl amide: effect on Pu(IV) complexes in solution. *Dalton Transactions* 2018, *47*, 1, 251-263. DOI:10.1039/c7dt03447d.

28 Matveev, P. I.; Mitrofanov, A. A; Petrov, V. G.; Zhokhov, S. S.; Smirnova, A. A.; Ustynyuk, Yu. A.; Kalmykova, S. N. RSC Adv., 2017, 7, 55441. DOI: 10.1039/c7ra11622e

29 Zhou,Z.; Parr, R. G.. Activation hardness: new index for describing the orientation of electrophilic aromatic substitution. Journal of the American Chemical Society, 112(15):5720-5724, 1990.

30 Pearson, R. G. Chemical hardness and density functional theory. Journal of Chemical Sciences, 117(5):369-377, 2005.

31 Korth, H. G.; Sicking, W. Prediction of methyl C-H bond dissociation energies by density functional theory calculations. *J. Chem. Soc.-Perkin Trans. 2* 1997, 4, 715-719. DOI:10.1039/a607177e.

32 Lee, C. T.; Yang, W. T.; Parr, R. G. Development of the Colle-Salvetti Correlation-Energy Formula into a Functional of the Electron-Density. *Phys. Rev. B* 1988, *37*, 2, 785-789. DOI:10.1103/PhysRevB.37.785.

33 Becke, A. D. Density-Functional Thermochemistry. III. The Role of Exact Exchange. *J. Chem. Phys.* 1993, *98*, 7, 5648-5652. DOI:10.1063/1.464913.

34 Elliott, P.; Burke, K. Non-Empirical Derivation of the Parameter in the B88 Exchange Functional. *Can. J. Chem.* 2009, *87*, 10, 1485-1491. DOI:10.1139/v09-095.

35 Wilden, A.; Kowalski, P. M.; Klaß, L.; Kraus, B.; Kreft, F.; Modolo, G.; Li, Y.; Rothe, J.; Dardenne, K.; Geist, A.; Leoncini, A.; Huskens, J.; Verboom, W. Unprecedented Inversion of Selectivity and Extraordinary Difference in the Complexation of Trivalent *f*-Elements by Diastereomers of a Methylated Diglycolamide. *Chem. Eur. J.* 2019, *25*, 21, 5507-5513. DOI:10.1002/chem.201806161.

36 Wilden, A.; Modolo, G.; Lange, S.; Sadowski, F.; Beele, B. B.; Skerencak-Frech, A.; Panak, P. J.; Iqbal, M.; Verboom, W.; Geist, A.; Bosbach, D. Modified Diglycolamides for the An(III) + Ln(III) Co-separation: Evaluation by Solvent Extraction and Time-Resolved Laser Fluorescence Spectroscopy. *Solvent Extr. Ion Exch.* 2014, *32*, 2, 119-137. DOI:10.1080/07366299.2013.833791.

37 Iqbal, M.; Huskens, J.; Verboom, W.; Sypula, M.; Modolo, G. Synthesis and Am/Eu Extraction of Novel TODGA Derivatives. *Supramol. Chem.* 2010, *22*, 11, 827-837. DOI:10.1080/10610278.2010.506553.

38 Hioe, J.; Zipse, H. Radical Stability and its Role in Synthesis and Catalysis. *Org. Biomol. Chem.* 2010, *8*, 16, 3609-3617. DOI:10.1039/c004166a.

39 Peng, C.; Schlegel, H. B. Combining synchronous transit and quasi-newton methods to find transition states. Israel Journal of Chemistry, 33(4):449-454, 1993.

40 Peng, C.; Ayala, P. Y.; Schlegel, H. B.; Frisch, M. J. Using redundant internal coordinates to optimize equilibrium geometries and transition states. Journal of Computational Chemistry, 17(1):49-56, 1996.

This project has received funding from the EURATOM research and training programme 2014-2018 under grant agreement No 755171. The content of this deliverable reflects only the author's view. The European Commission is not responsible for any use that may be made of the information it contains.

41 Li, X.; Frisch, M. J. Energy-represented direct inversion in the iterative subspace within a hybrid geometry optimization method. Journal of chemical theory and computation, 2(3):835-839, 2006.

42 M. J. Frisch, G. W. Trucks, H. B. Schlegel, G. E. Scuseria, M. A. Robb, J. R. Cheeseman, J. A. Montgomery, Jr., T. Vreven, K. N. Kudin, J. C. Burant, J. M. Millam, S. S. Iyengar, J. Tomasi, V. Barone, B. Mennucci, M. Cossi, G. Scalmani, N. Rega, G. A. Petersson, H. Nakatsuji, M. Hada, M. Ehara, K. Toyota, R. Fukuda, J. Hasegawa, M. Ishida, T. Nakajima, Y. Honda, O. Kitao, H. Nakai, M. Klene, X. Li, J. E. Knox, H. P. Hratchian, J. B. Cross, V. Bakken, C. Adamo, J. Jaramillo, R. Gomperts, R. E. Stratmann, O. Yazyev, A. J. Austin, R. Cammi, C. Pomelli, J. W. Ochterski, P. Y. Ayala, K. Morokuma, G. A. Voth, P. Salvador, J. J. Dannenberg, V. G. Zakrzewski, S. Dapprich, A. D. Daniels, M. C. Strain, O. Farkas, D. K. Malick, A. D. Rabuck, K. Raghavachari, J. B. Foresman, J. V. Ortiz, Q. Cui, A. G. Baboul, S. Cliord, J. Cioslowski, B. B. Stefanov, G. Liu, A. Liashenko, P. Piskorz, I. Komaromi, R. L. Martin, D. J. Fox, T. Keith, M. A. Al-Laham, C. Y. Peng, A. Nanayakkara, M. Challacombe, P. M. W. Gill, B. Johnson, W. Chen, M. W. Wong, C. Gonzalez, and J. A. Pople. Gaussian 09, Revision D.01. Gaussian, Inc., Wallingford, CT, 2004.

43 Garza, A. J. Solvation Entropy Made Simple. *J. Chem. Theory Comput.* 2019, *15*, 5, 3204-3214. DOI:10.1021/acs.jctc.9b00214.

44 Bondi, A. van der Waals Volumes + Radii. *J. Phys. Chem.* 1964, *68*, 3, 441-451. DOI:10.1021/j100785a001.

45 Galán, H.; Núñez, A.; Espartero, A. G.; Sedano, R.; Durana, A.; de Mendoza, J. Radiolytic Stability of TODGA: Characterization of Degraded Samples under Different Experimental Conditions. *Proc. Chem.* 2012, *7*, 195-201. DOI:10.1016/j.proche.2012.10.033.

46 Giannozzi, P.; Baroni, S.; Bonini, N.; Calandra, M.; Car, R.; Cavazzoni, C.; Ceresoli, D.; Chiarotti, G. L.; Cococcioni, M.; Dabo, I.; Dal Corso, A.; de Gironcoli, S.; Fabris, S.; Fratesi, G.; Gebauer, R.; Gerstmann, U.; Gougoussis, C.; Kokalj, A.; Lazzeri, M.; Martin-Samos, L.; Marzari, N.; Mauri, F.; Mazzarello, R.; Paolini, S.; Pasquarello, A.; Paulatto, L.; Sbraccia, C.; Scandolo, S.; Sclauzero, G.; Seitsonen, A. P.; Smogunov, A.; Umari, P.; Wentzcovitch, R. M. QUANTUM ESPRESSO: a modular and open-source software project for quantum simulations of materials. *J. Phys.-Condes. Matter* 2009, *21*, 39, 395502. DOI:10.1088/0953-8984/21/39/395502.

47 Perdew, J. P.; Burke, K.; Ernzerhof, M. Generalized Gradient Approximation Made Simple. *Phys. Rev. Lett.* 1996, *77*, 18, 3865-3868. DOI:10.1103/PhysRevLett.77.3865.

48 Sedrez, P. C.; Sanchez, C. J. N.; da Silva, M. J.; Barbosa, J. R. Dielectric Constant of Mixtures of Carbon Dioxide and *n*-Dodecane Between 283 K and 343 K. *Int. J. Thermophys.* 2020, *41*, 2, 16. DOI:10.1007/s10765-019-2597-y.

49 Petersson, G.; Bennett, A.; Tensfeldt, T. G.; Al-Laham, M. A.; Shirley, W. A.; Mantzaris, J. A complete basis set model chemistry. I. The total energies of closed-shell atoms and hydrides of the rst-row elements. The Journal of chemical physics, 89(4):2193-2218, 1988.

50 Petersson, G.; Al-Laham, M. A.; A complete basis set model chemistry. II. Open-shell systems and the total energies of the first-row atoms. The Journal of chemical physics, 94(9):6081-6090, 1991.

51 S. Miertuš, E. Scrocco, and J. Tomasi. Electrostatic interaction of a solute with a continuum. A direct utilizaion of AB initio molecular potentials for the prevision of solvent effects. Chemical Physics, 55(1):117-129, 1981.

52 J.-L. Pascual-ahuir, E. Silla, and I. Tunon. GEPOL: An improved description of molecular surfaces. III. A new algorithm for the computation of a solvent-excluding surface. Journal of Computational Chemistry, 15(10):1127-1138, 1994.

This project has received funding from the EURATOM research and training programme 2014-2018 under grant agreement No 755171. The content of this deliverable reflects only the author's view. The European Commission is not responsible for any use that may be made of the information it contains.

53 J. Tomasi, B. Mennucci, and R. Cammi. Quantum mechanical continuum solvation models. Chemical reviews, 105(8):2999-3094, 2005.

54 S. Grimme, J. Antony, S. Ehrlich, and H. Krieg. A consistent and accurate ab initio parametrization of density functional dispersion correction (DFT-D) for the 94 elements H-Pu. The Journal of chemical physics, 132(15):154104, 2010.

55 S. Grimme, S. Ehrlich, and L. Goerigk. Eect of the damping function in dispersion corrected density functional theory. Journal of computational chemistry, 32(7):1456-1465, 2011.

56 P. Pracht, F. Bohle, and S. Grimme. Automated Exploration of the low-energy Chemical Space with fast Quantum Chemical Methods. Physical Chemistry Chemical Physics, 2020.

57 S. Grimme, C. Bannwarth, and P. Shushkov. A robust and accurate tightbinding quantum chemical method for structures, vibrational frequencies, and noncovalent interactions of large molecular systems parametrized for all spdblock elements (Z= 186). Journal of chemical theory and computation, 13(5):1989-2009, 2017.

58 C. Bannwarth, S. Ehlert, and S. Grimme. GFN2-xTB - An accurate and broadly parametrized self-consistent tight-binding quantum chemical method with multipole electrostatics and density-dependent dispersion contributions. Journal of chemical theory and computation, 15(3):1652-1671, 2019.

59 P. Pracht, E. Caldeweyher, S. Ehlert, and S. Grimme. A Robust Non-Self-Consistent Tight-Binding Quantum Chemistry Method for Large Molecules. 2019.

60 S. Grimme. xtb doc Release 6.2. 2019.

61 A. McLean and G. Chandler. Contracted Gaussian basis sets for molecular calculations. I. Second row atoms, Z= 11-18. The Journal of Chemical Physics, 72(10):5639-5648, 1980.

62 R. Krishnan, J. S. Binkley, R. Seeger, and J. A. Pople. Self-consistent molecular orbital methods. XX. A basis set for correlated wave functions. The Journal of chemical physics, 72(1):650-654, 1980.

63 F. Weigend and R. Ahlrichs. Balanced basis sets of split valence, triple zeta valence and quadruple zeta valence quality for H to Rn: Design and assessment of accuracy. Physical Chemistry Chemical Physics, 7(18):3297-3305, 2005.

64 F.Weigend. Accurate Coulomb-fitting basis sets for H to Rn. Physical chemistry chemical physics, 8(9):1057-1065, 2006.

65 E. Glendening, J. Badenhoop, A. Reed, J. Carpenter, J. Bohmann, C. Morales, C. Landis, and F. Weinhold. Natural bond orbital analysis program: NBO 6.0. Theoretical Chemistry Institute, University of Wisconsin, Madison, WI, 2013.

66 J. W. Ochterski. Thermochemistry in gaussian. Gaussian Inc, 1:19, 2000.

67 Cížek, J. On the use of the cluster expansion and the technique of diagrams in calculations of correlation effects in atoms and molecules. Advances in chemical physics, pages 35-89, 1969.

68 R. J. Bartlett and G. D. Purvis. Many-body perturbation theory, coupledpair many-electron theory, and the importance of quadruple excitations for the correlation problem. International Journal of Quantum Chemistry, 14(5):561-581, 1978.

69 J. Pople, R. Krishnan, H. Schlegel, and J. Binkley. Electron correlation theories and their application to the study of simple reaction potential surfaces. International Journal of Quantum Chemistry, 14(5):545-560, 1978.

This project has received funding from the EURATOM research and training programme 2014-2018 under grant agreement No 755171. The content of this deliverable reflects only the author's view. The European Commission is not responsible for any use that may be made of the information it contains.

70 G. D. Purvis III and R. J. Bartlett. A full coupled-cluster singles and doubles model: The inclusion of disconnected triples. The Journal of Chemical Physics, 76(4):1910-1918, 1982.

71 J. A. Pople, M. Head-Gordon, and K. Raghavachari. Quadratic configuration interaction. A general technique for determining electron correlation energies. The Journal of chemical physics, 87(10):5968-5975, 1987.

72 G. E. Scuseria, C. L. Janssen, and H. F. Schaefer Iii. An e-cient reformulation of the closed-shell coupled cluster single and double excitation (CCSD) equations. The Journal of Chemical Physics, 89(12):7382-7387, 1988.

73 G. E. Scuseria and H. F. Schaefer III. Is coupled cluster singles and doubles (CCSD) more computationally intensive than quadratic conguration interaction (QCISD)? The Journal of Chemical Physics, 90(7):3700-3703, 1989.

74 F. Neese. The ORCA program system. Wiley Interdisciplinary Reviews: Computational Molecular Science, 2(1):73-78, 2012.

75 F. Neese. Software update: the ORCA program system, version 4.0. Wiley Interdisciplinary Reviews: Computational Molecular Science, 8(1):e1327, 2018.

76 F. Neese and F. Wennmohs. ORCA manual version 4.0.1. 2018.

77 S. Kossmann and F. Neese. Comparison of two e-cient approximate Hartee-Fock approaches. Chemical Physics Letters, 481(4-6):240-243, 2009.

78 R. Izsák, A. Hansen, and F. Neese. The resolution of identity and chain of spheres approximations for the LPNO-CCSD singles Fock term. Molecular Physics, 110(19-20):2413-2417, 2012.

79 B. Delley. An all-electron numerical method for solving the local density functional for polyatomic molecules. The Journal of chemical physics, 92(1):508-517, 1990.

80 B. Delley. From molecules to solids with the $DMol^3$ approach. The Journal of chemical physics, 113(18):7756-7764, 2000.

81 J. Tomasi and M. Persico. Molecular interactions in solution: an overview of methods based on continuous distributions of the solvent. Chemical Reviews, 94(7):2027-2094, 1994.

82 A. Klamt and G. Schüürmann. COSMO: a new approach to dielectric screening in solvents with explicit expressions for the screening energy and its gradient. Journal of the Chemical Society, Perkin Transactions 2, (5):799-805, 1993.

83 J. Tomasi and M. Persico. Molecular interactions in solution: an overview of methods based on continuous distributions of the solvent. Chemical Reviews, 94(7):2027-2094, 1994.

84 A. Klamt and G. Schüürmann. COSMO: a new approach to dielectric screening in solvents with explicit expressions for the screening energy and its gradient. Journal of the Chemical Society, Perkin Transactions 2, (5):799-805, 1993.

85 Litwinienko G, Ingold KU. Solvent Effects on the Rates and Mechanisms of Reaction of Phenols with Free Radicals. Acc. Chem. Res. 2007; 40:222–230. [PubMed: 17370994].

This project has received funding from the EURATOM research and training programme 2014-2018 under grant agreement No 755171. The content of this deliverable reflects only the author's view. The European Commission is not responsible for any use that may be made of the information it contains.